Optically detected magnetic resonance spectroscopic analyses on the role of magnetic ions in colloidal nanocrystals ⊘

Joanna Dehnel ; Adi Harchol ; Yahel Barak ; Itay Meir ; Faris Horani ; Arthur Shapiro ; Rotem Strassberg ; Celso de Mello Donegá ; Hilmi Volkan Demir ; Daniel R. Gamelin ; Kusha Sharma ✉ ; Efrat Lifshitz ✉

Check for updates

CrossMark

View Online   Export Citation

Articles You May Be Interested In

Are the homogeneous linewidths of spin resonance (ODMR) and optical transitions related?

J. Chem. Phys. (July 2008)

ODMR and resonance Raman spectroscopy of chlorophyll *b* on graphite

J. Chem. Phys. (June 1985)

On the nature of the relationship between inhomogeneously broadened phosphorescence and ODMR spectral lines

J. Chem. Phys. (May 1988)

AIP Publishing

Optically detected magnetic resonance spectroscopic analyses on the role of magnetic ions in colloidal nanocrystals

Joanna Dehnel,[1] Adi Harchol,[1] Yahel Barak,[1] Itay Meir,[1] Faris Horani,[1,2] Arthur Shapiro,[1,3]
Rotem Strassberg,[1] Celso de Mello Donegá,[4] Hilmi Volkan Demir,[5,6] Daniel R. Gamelin,[2]
Kusha Sharma,[1,a] and Efrat Lifshitz[1,a]

AFFILIATIONS

[1] Schulich Faculty of Chemistry, Solid State Institute, Russell Berrie Nanotechnology Institute,
Technion–Israel Institute of Technology, Haifa 3200003, Israel
[2] Department of Chemistry, University of Washington, Seattle, Washington 98195-1700, USA
[3] Optical Materials Engineering Laboratory, Department of Mechanical and Process Engineering, ETH Zurich,
8092 Zurich, Switzerland
[4] Condensed Matter and Interfaces, Debye Institute for Nanomaterials Science, Utrecht University,
3584 CC Utrecht, The Netherlands
[5] Luminous Center of Excellence for Semiconductor Lighting and Displays, TPI, School of Electrical and Electronic Engineering,
School of Physical and Mathematical Sciences, School of Materials Science and Engineering, Nanyang Technological
University–NTU Singapore, 639798, Singapore
[6] Department of Electrical and Electronics Engineering, Department of Physics, UNAM–Institute of Materials Science and
Nanotechnology, Bilkent University, Ankara 06800, Türkiye

Note: This paper is part of the JCP Special Topic on 40 Years of Colloidal Nanocrystals in JCP.
[a] Authors to whom correspondence should be addressed: kusha28793@gmail.com and ssefrat@technion.ac.il

ABSTRACT

Incorporating magnetic ions into semiconductor nanocrystals has emerged as a prominent research field for manipulating spin-related properties. The magnetic ions within the host semiconductor experience spin-exchange interactions with photogenerated carriers and are often involved in the recombination routes, stimulating special magneto-optical effects. The current account presents a comparative study, emphasizing the impact of engineering nanostructures and selecting magnetic ions in shaping carrier–magnetic ion interactions. Various host materials, including the II–VI group, halide perovskites, and I–III–VI$_2$ in diverse structural configurations such as core/shell quantum dots, seeded nanorods, and nanoplatelets, incorporated with magnetic ions such as Mn^{2+}, Ni^{2+}, and $Cu^{1+/2+}$ are highlighted. These materials have recently been investigated by us using state-of-the-art steady-state and transient optically detected magnetic resonance (ODMR) spectroscopy to explore individual spin-dynamics between the photogenerated carriers and magnetic ions and their dependence on morphology, location, crystal composition, and type of the magnetic ion. The information extracted from the analyses of the ODMR spectra in those studies exposes fundamental physical parameters, such as g-factors, exchange coupling constants, and hyperfine interactions, together providing insights into the nature of the carrier (electron, hole, dopant), its local surroundings (isotropic/anisotropic), and spin dynamics. The findings illuminate the importance of ODMR spectroscopy in advancing our understanding of the role of magnetic ions in semiconductor nanocrystals and offer valuable knowledge for designing magnetic materials intended for various spin-related technologies.

Published under an exclusive license by AIP Publishing. https://doi.org/10.1063/5.0160787

I. INTRODUCTION

Controlling the individual spins in semiconductor nanocrystals (NCs) is an emerging scientific field of the last decade that involves incorporating magnetic ions in host matrices to obtain diluted magnetic semiconductors (DMS).[1–3] These are generated by substituting some of the diamagnetic cations of the host lattice with magnetic ions (the so-called dopants). DMS compositions were already shown in a few different nanostructures in the past, like II–VI and III–V multiple quantum wells and self-assembled quantum dots (QDs),[4–6] transition metal dichalcogenides,[7] or nitrogen ions in diamond vacancies.[8] Those studies showed the creation of a large Zeeman splitting and Faraday rotation resulting from resident carrier-to-dopant spin exchange interactions.[9] However, a renaissance in the DMS field began during the past decade with the incorporation of magnetic ions into colloidal quantum structures,[10–13] a move that potentially enables the development of new spin-based technologies.[1,13]

Colloidal nanocrystals render size confinement down to a typical volume of ~300 nm^3 and show a relatively long (~10 ns) exciton radiative lifetime,[14,15] together markedly enhancing the carrier–dopant interaction with pronounced modification of the host's optical and magneto-optical properties.[10,16] Furthermore, the recently advanced synthesis procedures offer chemical controllability and flexibility in engineering the resident carriers' distribution and the allocation of the magnetic ions throughout various spatially confined morphologies in 0D to 2D regimes and hetero-composition (e.g., core/shell structures). Such engineering allows tuning of the strength and type of exchange interactions.[17,18] A few different synthetic methods have been introduced in recent years, including the use of single-source precursors,[19] cation exchange,[20] diffusion-controlled processes,[21] and layer-by-layer deposition during the kinetic growth stage.[22]

The most discussed colloidal DMS structures are based on the II–VI compounds. The band edges of common II–VI NCs are composed of the anion p-orbitals (valence band) and cation s-orbitals (conduction band). Therefore, the coupling of the unpaired spins of magnetic impurities with the band-edge states of II–VI semiconductors occurs via sp–d exchange interaction.[23,24] Magnetic ions from the first row of the transition metals are good candidates to supply individual spins: Mn^{2+} ($3d^5$, S = 5/2, L = 0), Ni^{2+} ($3d^8$, S = 1, L ≠ 0), Co^{2+} ($3d^7$, S = 3/2, L ≠ 0), and Cu^{2+} ($3d^9$, S = 1/2, L ≠ 0) for the free ions, each of which has a different occupation of its d-shell, with/without angular momentum or nuclear spins. Interactions such as spin–orbit coupling (SOC) (ions with L ≠ 0) and nuclear spin coupling may alter the sp–d exchange interaction and reduce the spin coherence time.[25] The electron–dopant coupling follows a potential spin-exchange interaction (positive energy), while the hole–dopant coupling corresponds to a kinetic spin-exchange interaction (negative energy).[2,26,27] Potential exchange interactions are always ferromagnetic (FM) and only weakly depend on the magnetic ion and host lattice.[28] Whereas, the kinetic exchange interactions can be either antiferromagnetic (AFM) or ferromagnetic (FM), depending on the occupation numbers in the d-shell of the magnetic ion and the particular location of the d-levels relative to the top of the valence band.[29–31] The host–guest interaction leads to a few different scenarios: (i) the existence of dopant states within the host energy bandgap directs a fast energy or charge transfer followed

by an atomistic d–d emission.[32] (ii) d-state positioning in resonance with or above band edge energies is dominated by the sp–d interaction, followed by an excitonic transition, while its strength strictly depends on the overlap between the host and guest carrier distribution functions.[33] In addition, spin exchange between a single exciton and a cloud of dopants induces the formation of a magnetic polaron.[2] (iii) If a single dopant state allocates within the energy gap, a plausible band-to-trap recombination is created (named below as metal-to-ligand charge transfer).[34]

A few pioneer groups exploring colloidal DMS quantum dots (QDs),[13,17,35–37] ribbons,[38] and nanoplatelets (NPLs)[39] embedded with Mn^{2+} and Cu^{2+} ions reported different observations disclosed from sp–d interaction and involving giant Zeeman splittings,[10,40] circular dichroism,[16,37] magnetic polaron formation,[12,41] fluctuation kinetics,[12,42,43] ion–ion interactions, and energy transfer processes.[44,45] Although a massive amount of work has been reported so far, there is a limited number of magneto-optical studies generally and a scarcity concerning anisotropic structures. Additionally, a few fundamental questions have been retained about the exact positioning of the dopant ions, the influence of dimensionality, the identification of individual spin exchange processes, and their radiative and spin relaxation processes.

To address these open issues, we thoroughly investigated spin degrees of freedom in colloidal NCs of different morphologies and compositions (see Fig. 1): Mn^{2+} doped in seeded rods of CdSe/CdS [Fig. 1(a)];[46] CdSe/CdS nanoplatelets [Fig. 1(b)];[47] Ni^{2+} doped in halide perovskites [Fig. 1(c)];[48] and $Cu^{1+/2+}$ doped in CdSe/CdS QDs in comparison with the role of Cu in $CuInS_2$ QDs [Fig. 1(d)].[49] The confined dimensions of these structures were anticipated to enhance the interaction between the resident photogenerated carriers and the guest magnetic ions either via the so-called sp–d spin exchange interaction or an energy/charge transfer process. The systems under investigation displayed a variety of dimensionalities from zero- to two-dimensional structures, unity, or hetero-structuring with
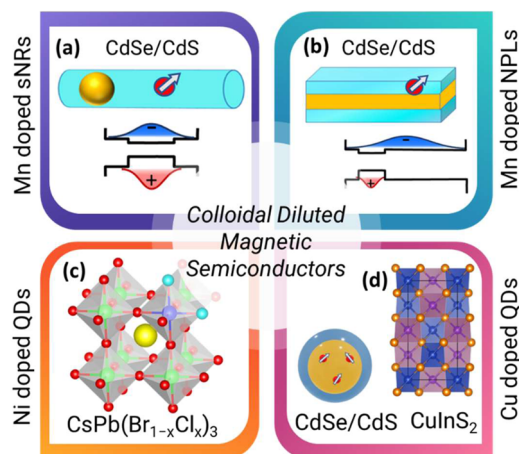

FIG. 1. Illustration of three different types of magnetic ions in colloidal semiconductor nanocrystals: Mn^{2+} doping in (a) CdSe/CdS seeded nanorods and (b) CdSe/CdS nanoplatelets. (c) Ni^{2+} doping in halide perovskites. (d) Cu^{2+}-doped CdSe/CdS quantum dots (left) and $CuInS_2$ (right).

d-orbital occupancy of the dopants. The mentioned studies implemented magneto-photoluminescence (PL) and optically detected magnetic resonance (ODMR) spectroscopies to illuminate the fundamental photo-physics and spin properties. The ODMR method provided important information on the exact location of host carriers and dopants and examined their interactions. The extracted physical parameters from the ODMR experiments included g-factors and their anisotropy, angular momentum, carrier–dopant coupling constants, radiative recombination mechanisms, and spin-lattice relaxation times, as explicitly explained in Sec. II. The current article brings a perspective on those discoveries by individually describing the investigation of four systems (see Sec. III), highlighting the implemented experimental principles and the resultant scientific evidence of carrier–dopant spin dynamics, and presenting relevant discussion (see Secs. III and IV). The synthesis and structural and compositional characterizations can be referred to in our previous publications.[46–49]

II. OPTICALLY DETECTED MAGNETIC RESONANCE

As mentioned in Sec. I, our studies explored the spin coupling between photogenerated carriers and dopant ions in the NC systems using steady-state and transient photoluminescence (PL) and

the corresponding optically detected magnetic resonance (ODMR) spectroscopies. However, before discussing the observations, a brief introductory explanation of ODMR spectroscopy is necessary to ease the readers' comprehension.

An ODMR experiment involves detecting magnetic resonance events at the excited state monitored as a differential change in the emission intensity, thus called optically detected magnetic resonance spectroscopy. Figures 2(a) and 2(b) illustrate schemes describing the involved radiative and magnetic resonance transitions in two relevant cases. In those, an electron (e) and a hole (h) are generated upon optical excitation when each carrier possesses a spin of $S = 1/2$ and a spin projection of $m_S = \pm 1/2$. Additionally, an applied static magnetic field (B_0) leads to Zeeman splitting of the carriers' spin states into a manifold comprised of two bright emitting states (blue horizontal lines) and two dark ones (gray horizontal lines). Simultaneously, microwave (MW) radiation is applied, which induces a spin–flip of the carriers (indicated by yellow and green arrows) from the dark to the bright states, conserving the $\Delta m_S = \pm 1$ transition selection rule. Exceptionally, a forbidden transition with $\Delta m_S = \pm 2$ may occur [light gray arrow in Fig. 2(b)]. As a note, the simple cases in Figs. 2(a) and 2(b) can, in principle, also represent a scenario involving carriers' spin greater than $1/2$. However, in this review, the discussion is mainly restricted to the scenarios depicted in Fig. 2.
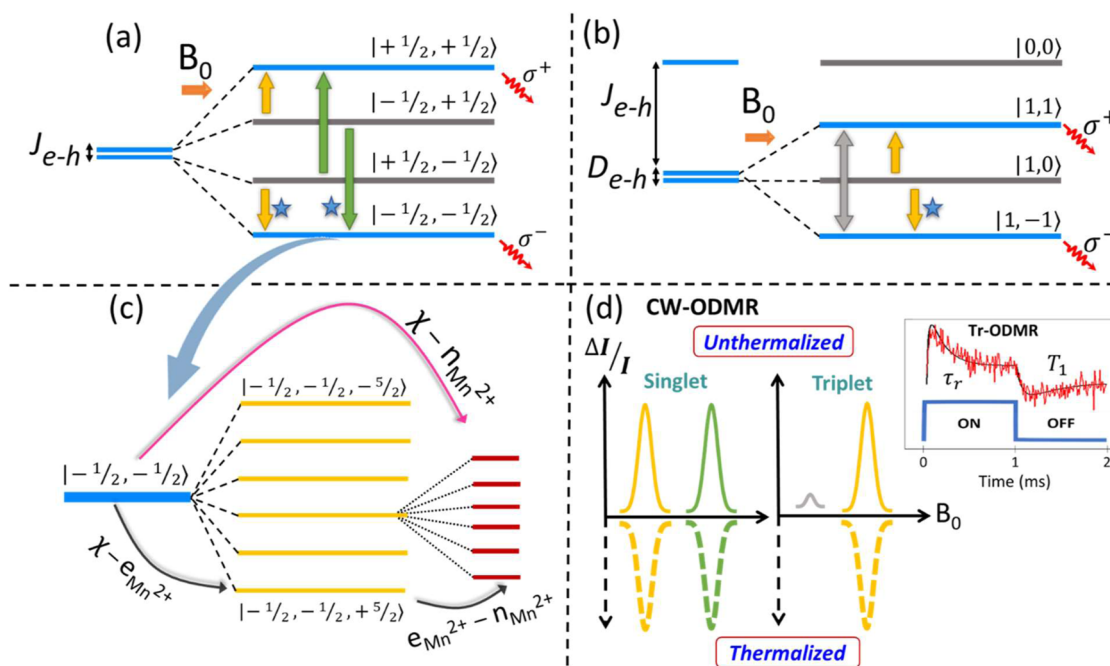
FIG. 2. (a, b) Schematic spin manifolds illustrating electrons and holes with $S = 1/2$ and a weak and strong exchange coupling (J_{e-h}), respectively. The spin manifold in (b) also includes zero field splitting (D_{e-h}). The red curly arrows represent the emission from the bright states to the ground state; the vertical yellow and green arrows represent the magnetic resonance transitions induced by MW irradiation for the electrons and holes, respectively; and the vertical light gray arrow in (b) represents the forbidden transition $\Delta m_S = \pm 2$. (c) Illustration of the coupling between an exciton (χ) and the nuclear spin of Mn^{2+} via two separate routes marked by pink and black arrows. In panels (a)–(c), the spin projections of the electron (m_e), hole (m_h), and dopant (m_{dopant}) are given in Dirac notations, $|m_e, m_h\rangle$ and $|m_e, m_h, m_{dopant}\rangle$. In addition, the horizontal blue lines (in (a)–(c)) denote bright states, and the horizontal gray lines in panels (a) and (b) denote dark states, and the horizontal yellow and red lines in panel (c) represent the Mn^{2+} electron and nuclear spin states. (d) Scheme of CW-ODMR spectra of the singlet and triplet cases. The positive (negative) signals refer to the unthermalized (thermalized) case. The yellow and green resonances represent the envelope of transitions corresponding to a spin flip of electrons and holes, respectively, as depicted in panels (a) and (b). The inset shows a typical time-resolved (Tr) ODMR spectrum for an unthermalized case, designating, respectively, the dominance of radiative (τ_R) and spin (T_1) relaxation times during the "on" and "off" periods of the MW pulse.

The magnetic resonance transitions manipulate the population of the emitting states, leading to a change in the PL intensity (red curly arrows). Consequently, an ODMR spectrum is obtained by plotting the change in the PL intensity ($\Delta I/I$) vs the strength of B_0.

Figures 2(a) and 2(b) differ in their e–h spin exchange interactions (J_{e-h}) and zero-field splitting (D_{e-h}) constants at $B_0 = 0$. In the case of a relatively weak J_{e-h} [panel (a)], a *singlet* emission is induced, whereas a substantially stronger J_{e-h} leads to *triplet* recombination [panel (b)]. Furthermore, each carrier is sensitive to the local crystal field (i.e., $D_{e-h} \neq 0$), as evidenced by a splitting of states in the spin manifold at $B_0 = 0$ and anisotropy in the g-factor. Additionally, the coupling of the carriers to the electron or nuclear spins of the dopants may appear as a splitting of the resonance or its broadening, as depicted in Fig. 2(c). It is important to note that the exciton (χ) coupling to a nuclear spin may follow two different routes, either via a direct coupling (χ–n) or mediated through electron coupling (χ–e + e–n).

Figure 2(d) shows anticipated continuous-wave (CW) ODMR spectra for singlet and triplet emission processes in correspondence with magnetic resonance transitions shown in Figs. 2(a) and 2(b), respectively. The sign of the ODMR signals reflects whether there is an increase or decrease in the population of the emitting states after a magnetic resonance event. When the recombination process occurs rapidly (τ_R) compared to the carriers' spin relaxation time (T_1), a gradient in population is created between the dark and bright states, known as an unthermalized process. Consequently, the magnetic resonance transitions depicted by the arrows in panels (a) and (b) enhance the emission intensity. This is pronounced as two positive resonances in the ODMR spectrum [solid lines in Fig. 2(d)], each containing the overlap of two spin flip events of the electron (yellow) and hole (green).

Conversely, a Boltzmann distribution is formed among the manifold' states for a radiative time in the range $\tau_R \geq T_1$, named here a thermalized process. This condition dictates magnetic resonance transitions from the lowest energy state to those above, hence inverting the resonance transitions specifically marked by stars in Figs. 2(a) and 2(b), which depletes the population of the lowest bright state. Since the contribution from the upper bright state is minor compared to the lower state, the ODMR spectrum appears as a negative signal in both singlet and triplet cases [dashed lines in Fig. 2(d)]. Ultimately, the resonances' pattern and sign provide steady-state and temporal information about the recombination mechanism.

The identifications of the involved carriers in the ODMR spectra are of paramount importance and can be quantified by simulating the spectra using a general spin Hamiltonian as described by the following equation:[50]

$$H_s = \sum_i \mu_B \vec{S}_i \overline{\overline{g}}_i \vec{B}_0 + \sum_{i \neq j} J_{i-j} \vec{S}_i \vec{S}_j + \sum_m A_{e,h-m} \vec{S}_{e,h} \vec{I}_m + \vec{S}_e \overline{\overline{D}}_{eh} \vec{S}_h. \quad (1)$$

In this equation, i and j represent the different spin species: electrons, holes, and dopants. The first term describes the Zeeman interaction, where μ_B is the Bohr magneton, S_i is the spin quantum number of species i, and g_i corresponds to its g-factor. The second term is the exchange coupling (J_{i-j}) between the spins of species i and j. The third term describes the hyperfine interaction (A) between the spins of electrons or holes and the nuclear spin, I_m. The last term is zero-field splitting (D_{e-h}).

Practically, in an ODMR experiment, the sample is placed within an MW cavity, positioned at the center of a magnetic coil, both of which have access to optical radiation. The emission is detected either in a Faraday configuration ($B_0 \parallel excitation$) or a Voigt configuration ($B_0 \perp excitation$), reflecting the selection rule for recombination emission. The MW magnetic field component (B_1) is always oriented normal to B_0 and is chopped at various frequencies, ranging from 40 to 10 000 Hz, enabling lock-in detection. Consequently, two experiments can be carried out: (i) averaging the values of $\Delta I/I$ emanated from numerous MW pulses during their "*on*" time. This mode provides a steady-state spectrum named a CW-ODMR, as illustrated in Fig. 2(d); and (ii) monitoring the $\Delta I/I$ value throughout the complete cycles of MW modulation ("*on*" and "*off*" times), commonly named a time-resolved (Tr) ODMR trend, as shown in the inset of Fig. 2(d). For practical reasons, transient information in this study was extracted by recording CW-ODMR spectra at various MW modulation frequencies instead of time-resolved traces, as these are Fourier transforms of each other. For the MW frequency-dependent measurements, CW-ODMR spectra were recorded both in-phase (IP) and out-of-phase (OP) relative to the turn-on time of the MW. The IP period supplies information about the radiative decay time (τ_R), while the OP period uncovers the spin-relaxation time (T_1), i.e., the recovery time of the signal after a spin–flip event [compatible with the time domains as indicated in the inset of Fig. 2(d)]. The ODMR MW modulation frequency dependence was simulated using a kinetic model, which allowed for the investigation of spin dynamics, particularly the spin-relaxation times. The implemented kinetic equation can be referred to in the Methods below and Ref. 51.

III. RESULTS AND DISCUSSION

A. CdSe/Cd$_{1-x}$Mn$_x$S core/shell colloidal seeded nanorods

As discussed earlier, magnetic doping has been extensively implemented in colloidal quantum dots, with limited work on anisotropic structures such as seeded nanorods (sNRs), wherein the latter possess significant properties such as reduced Auger rates[52,53] and tunability of electronic structure through a change in composition and length-to-width aspect ratio.[54,55]

Although the optical and electrical properties of sNRs have been thoroughly investigated in recent years, the spin degrees of freedom of those structures have been studied only to a lesser extent. A seminal work exposed the exciton fine structure of sNRs and discussed spin–flip processes among the exciton manifold.[56,57] Another related work reported the investigation of spin properties in simple rods and in undoped core/tetrapod heterostructures.[58,59] Nevertheless, only one report exposed the spin and magneto-optical properties of diluted magnetic sNRs.[21] Notably, none of the mentioned studies addressed the impact of the core–shell interface on the spin degree of freedom in these elongated structures, and neither exposed the interaction of magnetic dopants with trapped carriers at interface sites.

Here, we aim to summarize the study on spin properties in a colloidal CdSe/Cd$_{1-x}$Mn$_x$S seeded-nanorod (sNRs) structure doped with a dilute concentration of Mn^{2+} ions across the rods. The studied sample comprised a core with a diameter of 3.1 nm and rod

dimensions of 30 × 4 nm^2 with an Mn concentration of x = 0.01. Those dimensions correspond to a type-I core-to-rod band alignment, endowing confinement of both photoexcited electrons and holes within the core regime [see scheme in Fig. 1(a)].

Figure 3(a) displays a low-temperature photoluminescence (PL) spectrum of doped sNRs, spread over two distinct spectral regimes, associated with exciton (green) and trap (red) recombination processes, and showing only minor changes with respect to those of pure sNRs (not shown here). The PL decay curves corresponding to the green and red bands are displayed in the inset. A fit to the dominant components in the green region revealed a lifetime of 38.1 ns (15.6 ns for undoped), while the red region exhibits a dominant component with a lifetime of 634 ns (514 ns for undoped). The extension of the lifetime observed in doped sNRs can be ascribed to either interaction between photogenerated carriers and Mn-dopant or the self-trapping of carriers induced by distortions around the dopants.[11]

The spin properties of the green and red emission processes were further studied with their association with the dopant's spins measured by CW and frequency-dependent ODMR spectroscopy. Figure 3 presents CW-ODMR spectra of undoped and doped sNRs, recorded selectively across the green or red spectral regimes
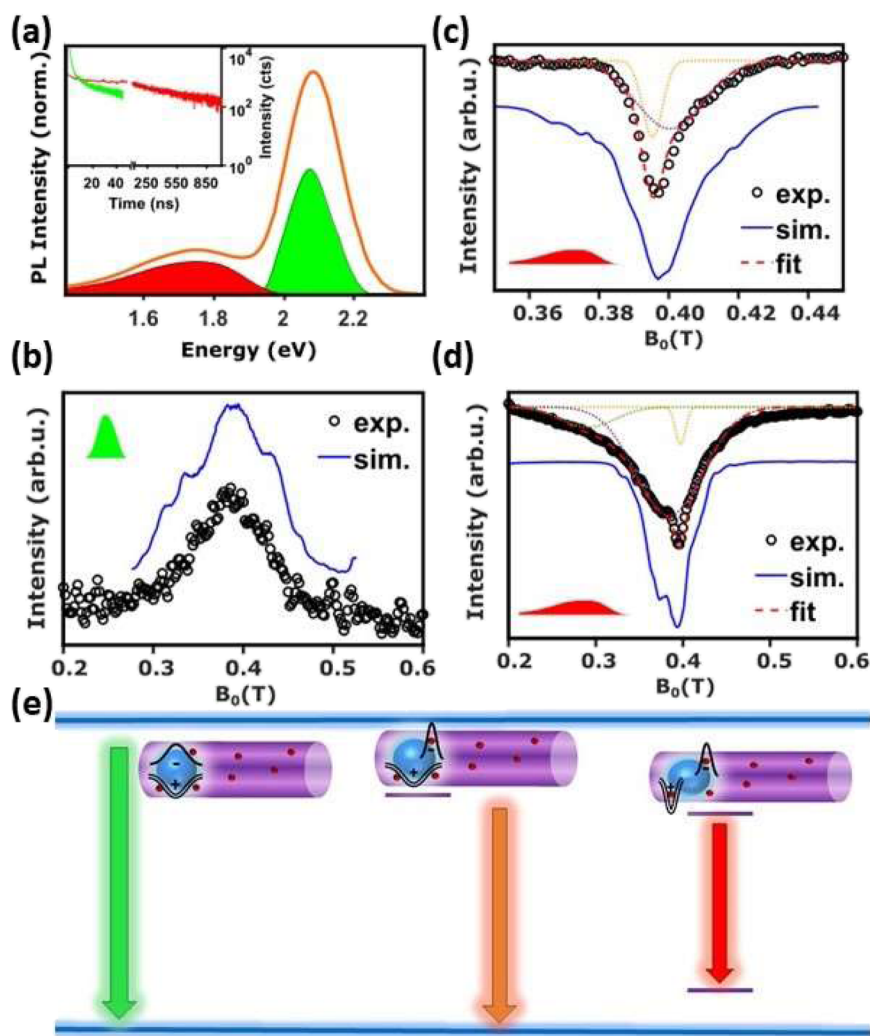
FIG. 3. (a) PL spectrum of CdSe/Cd$_{1-x}$Mn$_x$S sNRs recorded at 2.17 K. The overlapping green and red bands correspond to the spectra recorded through different optical filters. Inset: PL decay curves of the green and red emission bands. ODMR spectra of (b) CdSe/Cd$_{1-x}$Mn$_x$S sNRs monitored at the green-emission region, (c) CdSe/CdS sNRs, and (d) CdSe/Cd$_{1-x}$Mn$_x$S sNRs monitored at the red-emission regions. (e) Scheme of recombination processes evolved from the ODMR investigation: The arrows mark the band-to-band (green), trap-to-band (orange), and trap-to-trap (red) recombination processes. The relevant carriers' wavefunctions' are displayed schematically. The observed ODMR spectrum related to each emission event is displayed above each arrow. Reproduced with permission from Dehnel *et al.*, ACS Nano **14**, 13478–13490 (2020). Copyright 2020 American Chemical Society.

(see color LOGOs at the insets). The ODMR spectrum across the green region of doped sNRs [Fig. 3(b)] is dominated by a positive resonance with a weak fine structure. Notably, the exciton transition in the corresponding undoped sample did not present any ODMR signal. The ODMR spectrum of the red band in undoped sNRs [Fig. 3(c)] consists of a broad negative resonance fitted by double Gaussian functions (thin lines). The corresponding band in the doped sNRs [Fig. 3(d)] spectrum consists of three distinguished negative resonances (see dashed lines): a sharp one at the same field as that found in the undoped sample, a broad one with a weak fine structure, and another weak resonance at the lowest field. As indicated in Sec. II, the negative signals correlate with a thermalized event with a slow recombination emission, presumably due to the existence of at least one trapped carrier. In contrast, the positive signal, recorded in the green spectral regime (the exciton process), involved a fast recombination emission and acted as an unthermalized process.

The ODMR observations were simulated using a spin Hamiltonian, as discussed in Sec. II. Note that the simple evaluation of the number of Mn^{2+} ions in close proximity to the interface given in Ref. 46 reveals ~21 dopant ions out of 1718 metal sites. Such a dilution supports the assumption considered in the simulation for the interaction of a single Mn^{2+} ion with a single trapped carrier at the interface. The most critical magnetic parameters bestowed through the simulation of the CW-ODMR spectra are summarized in Table I. The simulations of the spectra related to the red-PL bands in doped/undoped samples exhibit anisotropy in the Landé g-factors deviating from the values found for carriers in the band edges of the host lattice. Such a deviation designates the allocation of a

carrier at a trapping site, presumably around the seed/rod interface. Based on the absolute values as well as their anisotropy, a few different radiative recombination processes were proposed [see a scheme in Fig. 3(e)]. The green emission is associated with band-to-band recombination, including a minor distribution of their wavefunctions across the core/rod boundary, and those permits remain intact with nearby Mn^{2+} dopants. An orange emission corresponds to trap-to-band recombination, which is featured for both undoped and doped sNRs. A red, deep emission belongs to a trap-to-trap emission, proposing the trapping of both electrons and holes at the interface. Notably, the trap-to-trap resonance transition shifted from $g = 1.903$–2.002 for doped sNRs, supporting the association of this shift to the coupling between carriers located at the core/rod interface and the magnetic impurities in the nearest region.

Table I exposes a few intriguing facts about other parameters beyond the g-factors. One of which is the spin exchange interactions between the electron–Mn^{2+} ($J_{e\text{-}Mn}$) and hole–Mn^{2+} ($J_{h\text{-}Mn}$), which should depend on the Laporte selection rules ($\Delta L = \pm 1$) and the mutual distribution function overlap. Those variables were found to be in the 100 μeV range, albeit with a stronger coupling of the hole-Mn^{2+} pair, as commonly observed in II–VI semiconductors. Such a coupling becomes possible for carriers with some degree of distribution across the core/rod interface since the Mn^{2+} was selectively positioned at the rod constituent.

Furthermore, the ODMR measured was recorded under different MW modulation frequencies to deconvolve overlapping events and extract temporal information. Figure 4(a) presents a set of CW-ODMR spectra recorded under selective MW modulation frequencies (see legends). This set includes IP (solid lines) and OP

TABLE I. Fit parameters for simulating the ODMR spectra using the spin Hamiltonian [Eq. (1)] and kinetic model [Eq. (4)].

	CdSe/Cd$_{1-x}$Mn$_x$S sNRs[a]	CdSe/Cd$_{1-x}$Mn$_x$S NPLs	Ni-doped perovskites	Cu-doped CdSe/CdS QDs	CuInS$_2$ QDs
g_e	$g_{xx} = g_{yy} = 1.99$ $g_{zz} = 1.76$	$g_{xx} = g_{yy} = 1.90$ $g_{zz} = 2.10$	$g_{xx} = g_{yy} = g_{zz} = 1.99$	$g_{xx} = g_{yy} = 1.73$ $g_{zz} = 1.74$	Bound exciton $g_{xx} = g_{yy} = 1.81$
g_h	hh $g_{xx} = g_{yy} = -1.04$[b] $g_{zz} = -1.02$ th $g_{xx} = g_{yy} = 1.32$[b] $g_{zz} = -1.28$	$g_{xx} = g_{yy} = -0.48$ $g_{zz} = -0.67$	$g_{xx} = g_{yy} = 1.14$ $g_{zz} = 1.12$	$g_{xx} = g_{yy} = 1.76$ $g_{zz} = 1.91$	$g_{zz} = 1.96$
$J_{e\text{-}h}$ (μeV)	hh 0.1[b] th 0.93[b]	0.8	0.1	0.1	1 meV
$J_{e\text{-}dopant}$ (meV)	0.03	0.76	⋯	⋯	⋯
$J_{h\text{-}dopant}$ (meV)	−0.19	−0.54	0.002	⋯	⋯
$D_{e\text{-}h}$ (μeV)	⋯	⋯	⋯	⋯	19
$A_{e.h\text{-}nuclei}$ (μeV)	−0.7	−0.51	⋯	2.4	
T_1 (ms)	0.1	1.0	e − 0.2 h - 0.75	e − 0.82 h - 0.11	Bound exciton 0.23

[a]Fit parameters for the simulation of the red emission.
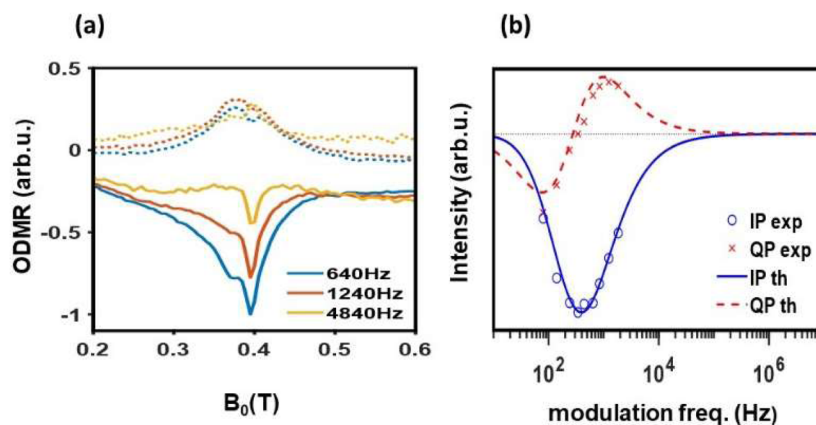[b]hh – heavy hole. th – trapped hole.

FIG. 4. (a) IP and OP ODMR spectra of CdSe/Cd$_{1-x}$Mn$_x$S sNRs monitored at the red-emission region under various MW modulation frequencies. (b) Integrated ODMR intensity as a function of the MW modulation frequency for the IP (blue circles) and OP (red crosses) signals. Reproduced with permission from Dehnel *et al.*, ACS Nano **14**, 13478–13490 (2020). Copyright 2020 American Chemical Society.

(dashed lines) measurements with respect to the turn-on time of the MW pulse. The evolution of the spectra with the change in modulation frequency unprecedentedly uncovers the existence of more than one resonance type. Figure 4(b) displays the analysis of the MW-modulation dependence by plotting the integrated intensity of each component in the ODMR spectra vs the frequency for the IP (blue symbols) and OP (red symbols) detections. The observed trends were further analyzed by simulating the data using the kinetic equations described in Sec. V. The results of these simulations are presented as the blue line and red dashed line in Fig. 4(b). One of the most critical parameters emanating from those fits is the spin-relaxation time (T$_1$), which shows a relatively long spin-relaxation time (0.1 ms) in doped sNRs compared to their undoped analog (0.01 ms). The relatively long T$_1$ values are commonly found in cases where the examined carriers are free from spin–orbit coupling (SOC), like the trapped carriers in the present case, which are detached from the orbit effect of the valence band. Moreover, an order of magnitude gap in spin-relaxation time upon doping further supports the evidence of magnetic coupling between interface carriers and neighboring Mn^{2+} ions.

As an intermediate summary, the comparison between the pristine structures (CdSe/CdS) and the magnetically doped derivative, CdSe/Cd$_{1-x}$Mn$_x$S, indicated that both include trapping of the photogenerated carriers at the interface between the seed and the rod. The trapped carriers possess unpaired spins (S = 1/2) that endow selective magneto-optical properties with extended radiative and spin-relaxation times. The dominant interaction with the magnetic dopant occurs along the seed/rod interface, further enhancing spin helicity and the radiative lifetime and, most importantly, an order of magnitude extension of spin-lattice relaxation time.

B. CdSe/Cd$_{1-x}$Mn$_x$S core/shell colloidal nanoplatelets (NPLs)

Colloidal semiconductor NPLs, in contrast to QDs, exhibit a distinct characteristic of pure tight confinement along their vertical thickness and strongly exhibit thickness-dependent electronic structure and optical properties. In addition, due to great efforts in recent years, the synthesis of NPLs with atomically flat surfaces effectively suppresses inhomogeneous broadening. This enables the achievement of extremely narrow emission bandwidths and a large absorption cross-section.[60] Furthermore, colloidal controllability and flexibility make the synthesis of NPLs of different thicknesses with atomic precision possible.[61] This allows precise control and uniform distribution of the magnetic dopants, unlike their spherical counterparts, which often face challenges such as size variations and non-uniform distribution of dopants.[62]

Magneto-optical investigations on two-dimensional magnetically doped NCs such as nanoplatelets[39] and nanoribbons[38,63] have been documented in previous research and have shown the generation of a large Zeeman splitting because of the resident spin-exchange interactions between the carrier and the dopant. However, independent evaluation of the s–d and p–d exchange interactions using the advantages of the core/shell heterostructures has been studied to a limited extent.

In this study, the examined NPLs consisted of a core platelet with thickness/length/width dimensions of 0.7 nm/30 nm/20 nm, and a shell platelet with a thickness varying from 0.35 to 1.4 nm and an Mn concentration of x = 0.01. These quantum platelets possess a quasi-type-II band alignment, such that the photoexcited hole resides in the core region while the conduction-band electron can be distributed across the NPLs, enabling possible carrier-Mn s–d exchange interaction [see Fig. 1(b)].

Circularly polarized magneto-PL spectroscopy was employed to track the induced magnetization and the change in g-factor by incorporating Mn^{2+} dopants into the host CdSe/CdS NPL shell regime. The circularly polarized PL spectra were recorded in the presence of an external magnetic field. The data were then plotted as the degree of circular polarization [DCP = $(I_{\sigma+} - I_{\sigma-})/(I_{\sigma+} + I_{\sigma-})$] vs the strength of the applied magnetic field (from 0 to 8 T), as shown in Fig. 5(a). The curves were fitted according to Eqs. (2) and (3) for the undoped and doped NPLs, respectively,
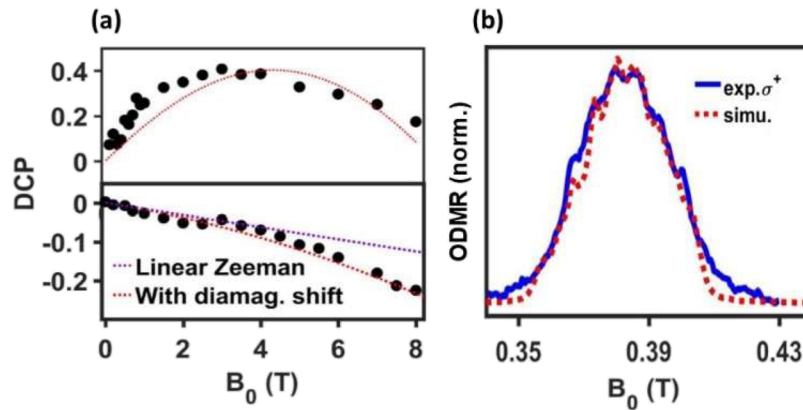
FIG. 5. (a) Plot of the degree of circular polarization vs the strength of an external magnetic field B_0 of CdSe/Cd$_{1-x}$Mn$_x$S (top panel) and CdSe/CdS (bottom panel) NPLs. The fitted dashed lines were calculated according to Eqs. (2) and (3) for the undoped and doped NPLs, respectively; (b) The ODMR spectrum of magnetically doped CdSe/Cd$_{1-x}$Mn$_x$S NPLs (solid blue curves) recorded under Faraday configuration and monitored with a circular polarizer σ^+ at 2.4 K. The dashed red curve corresponds to the best fit to one polarization direction calculated using the spin Hamiltonian in Eq. (1). Reproduced with permission from Strassberg *et al.*, J. Phys. Chem. Lett. **10**, 4437–4447 (2019). Copyright 2019 American Chemical Society.

$$DCP = -(\Delta E_z / 2k_B T), \qquad (2a)$$

$$DCP = -P_0 \tanh\left(\frac{\Delta E_z}{2k_B(T + T0)}\right). \qquad (2b)$$

P_0 in Eq. (2b) is a pre-factor that considers the random orientation of the NPLs in an ensemble. The exciton Zeeman splitting, ΔE_z, for the undoped NPLs is given by

$$\Delta E_z = g_{ex}\mu_B B_0 + \gamma B_0^2, \qquad (2c)$$

where the first term is the linear Zeeman contribution, while the second term is a diamagnetic shift. The variable γ is a diamagnetic shift coefficient, given as

$$\gamma = e^2 \langle r^2 \rangle / 8\mu, \qquad (2d)$$

where r is the Bohr radius of the electron, which is nearly the same as that of the exciton in II–VI semiconductors with a heavy hole and a light electron, and μ is the exciton's reduced mass ($1/\mu = 1/m_e + 1/m_h$).

For the doped NPLs, the expression ΔE_Z was replaced with

$$\Delta E_{z(Mn)} = g_{ex}\mu_B B_0 + \gamma B_0^2 + 1/2 x N_0 (f_e \alpha - f_h \beta) \langle S_{0,z}^{Mn} \rangle, \qquad (3)$$

in which the additional third term describes the splitting due to carrier–dopant spin-exchange interactions, where α and β are the electron–dopant and the hole–dopant exchange constants, N_0 is the number of cations per unit volume, f_e, f_h are the average overlap of the electron and hole wave functions with the Mn^{2+}, and $S_{0,z}$ is the average value of the Mn^{2+} spin projection on the laboratory axis z. The best-fit variables are summarized in Table II.

Figure 5(a) displays fitted curves for the experimental data points, revealing a g_{eff} = −4.1 for the doped NPLs (top panel) and a g_{ex} = +0.21 for the undoped NPLs (bottom panel). Therefore, the g-factor of magnetically doped NPLs differs from that of undoped NPLs in both absolute value and sign. The differences agree with other studies on magnetically doped nanocrystals.[48,49] In other words, such behavior reflects the sp–d interaction in the presence of a magnetic dopant.

Magnetic interactions were further characterized by utilizing ODMR spectroscopy. In the control experiment performed on the undoped sample, a single resonance band was observed (not shown here; the reader is directed to Ref. 47) and correlated with the spin–flip of a localized photogenerated electron by an interface potential. This result agrees with previous ODMR work carried out by the Lifshitz group,[50,64] which showed typical core/shell trapping sites, such as cation or anion vacancies (e.g., V$_{Cd0}$, V$_{S0}$). Figure 5(b) illustrates the ODMR spectrum of doped CdSe/Cd$_{1-x}$Mn$_x$S NPLs. The spectrum shows an envelope band centered at ~0.38 T with a pronounced sextet manifold and an average intra-sextet energy gap of 0.75 μeV. The measured intra-sextet energy gap value is slightly smaller than that found in the ESR measure (0.8 μeV) (not shown here), indicating a correlation between the trapped resident carrier and Mn nuclear spins. Such an interaction would occur across a volume with a radius equal to that of the exciton (~3 nm). A simple estimation discussed in a previous paper[47] approximated the

TABLE II. The best-fit physical parameters of CdSe/Cd$_{1-x}$Mn$_x$S using Eqs. (2) and (3).

Parameter	Value
S_0	5/2
g_{Mn}	2.0
$N_0\alpha$	0.22 eV
$N_0\beta$	−1.28 eV
f_e	0.63
f_h	0.08
T_0	9 K

existence of ~3 Mn atoms in the frame of the exciton across the core/shell interface.

This observation can be explained by the diagram shown In Fig. 2(c). The Mn^{2+} ion has a total electron spin of S = 5/2 and an observed characteristic sextet related to the ±1/2 of the Mn^{2+}-electron spin transition split by a nuclear-electron hyperfine interaction (with a nuclear spin of I = 5/2). The interaction of the exciton with the nuclear spin can occur either by a direct route, as shown by the pink arrow in Fig. 2(c), or by an indirect process mediated via the carrier-to-Mn^{2+} electron coupling, as displayed by the black arrows.

Based on the above arguments and the quantitative evolution derived from the spin Hamiltonian (see Table I), the experimental observations provided persuasive evidence for a hyperfine interaction between a localized electron at a trap interface site and the nuclear spins of the next neighboring Mn^{2+} ions localized at the core/shell interface. Moreover, the study was extended to investigate spin dynamics using the MW modulation frequency-dependent ODMR experiment, similar to the approach used to study sNRs. Such an experiment revealed a carrier–dopant spin relaxation time (T_1) of ~2.5 ms in undoped NPLs and 1 ms in doped NPLs. This observation demonstrated contradictory behavior compared to what was observed for sNRs, as doped NPLs exhibited shorter spin relaxation. These results further supported the observation of the coupling between the interface-trapped electron and nuclear spins, which partially suppresses the spin relaxation time.

In conclusion, the coupling to a nuclear spin may occur via a direct or indirect process, bridged by the resident-electron to guest-electron spin-exchange interaction [see Fig. 2(c)]. The contribution of nuclear spin has hardly been discussed for DMS nanostructures to date. This study highlighted the nuclear spin effect in DMSs, indicating that such interactions influence the carriers' spin coherence time. Therefore, this work reveals a crucial physical effect directly impacting spin-based applications.

C. Ni^{2+} doped lead-halide perovskites

The halide perovskite semiconductors under consideration have a chemical formula ABX_3 (A = counter ions: Cs, CH_3NH_3; B = Pb, Sn; X = I, Cl, Br). They are composed of metal-halide octahedrons that share edges, forming cages filled with small organic or inorganic countercations. Those materials have attracted significant scientific and technological interest due to their intriguing properties such as self-healing,[65] tolerance to defects,[66–68] long carrier diffusion lengths,[69] near-unity emission quantum yields,[70] large phonon anharmonicity,[68,71] strong carrier–phonon coupling, and polaron formation,[72] all of which dictate the electrical and optical phenomena of the materials.

The electronic band structure of $APbX_3$ is established by an inorganic network when the valence band is mainly composed of an s-orbital of metal and a p-orbital of halides, whereas the conduction band is mainly composed of p-orbitals of metal. The major contribution of heavy metal to the conduction band results in a spin–orbit coupling that lifts the p-orbital energy degeneracy, leaving both the conduction and valence band edges with a spin of $S_e = S_h = 1/2$.

Lately, magnetic doping in halide perovskites has been brought about by embedding transition metals or lanthanide cations (M) into the host lattices ($APbX_3$ structures),[73–75] which gives rise to structural stability emanating from the fact that these ions induce a stronger M–X interaction with respect to that of Pb-X, thus shrinking the octahedron sides and, subsequently, reducing the counter ion's motion (A). Remarkably, such impurities act silently on their magnetic properties.[76,77] However, as they endow the hosts with structural stability,[74,75,78] the impurities enable internal energy transfer from band-edge host states into their atomistic ligand field states, leading to a dual emission at various spectral regimes.

Recent studies on Ni doping described the general influence of the ions on the host properties, showing significant improvements in emission quantum yields, absorption and emission spectral shifts, and the extension of radiative lifetimes with respect to the undoped hosts.[79–83] However, despite the significant interest in doped halide perovskite NCs, there is still a lack of critical knowledge about the dopants' effect on these materials' magneto-optical properties. Here, we implemented ODMR for the first time to study the influence of magnetic doping on halide perovskite properties.

This section describes a recent investigation on the magneto-optical properties of Ni^{2+} doped cesium lead halide perovskites. The cube-shaped NCs have an average size of ~9 nm with the chemical formula $CsPb_{0.98}Ni_{0.02}(Br_{0.49}Cl_{0.51})_3$.
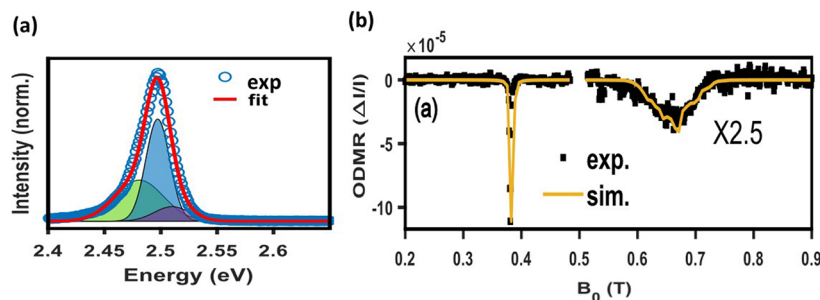
FIG. 6. (a) PL spectrum of Ni^{2+} doped $CsPb(Br_{1−x}Cl_x)_3$ NCs recorded at 4 K with Gaussian best-fit curves (purple, blue, and green). (b) ODMR spectrum of Ni^{2+} doped $CsPb(Br_{1−x}Cl_x)_3$ NCs while monitoring the full PL spectral range. The experimental raw data are shown by the black symbols and the spin Hamiltonian simulation by the yellow line. Reproduced with permission from Barak et al., Chem. Mater. **34**, 1686–1698 (2022). Copyright 2022 American Chemical Society.

Figure 6(a) depicts a PL spectrum of Ni^{2+} doped $CsPb(Br_{1-x}Cl_x)_3$ nano-cubes, recorded at 4 K. The spectrum is composed of an asymmetric band. The Gaussian fit reveals the origin of three components: one having an extremely fast radiative lifetime (~picoseconds) and two others (green and blue) with nanosecond decay times. The extended lifetime processes were associated with localized or trapped carriers induced by the presence of the dopants.

Figure 6(b) displays the ODMR spectrum of the emission band shown in panel (a). The spectrum reveals a dominant, sharp, and negative resonance centered at 0.38 T and an additional weak and broad band centered at 0.67 T. The average g-factors associated with the obtained bands were extracted from the simulation of the spectrum with a spin Hamiltonian as in Eq. (1) and were found to be 2.01 and 1.15 for low- and high-field resonances, respectively. These values deviated from those of the band-edge carrier (i.e., $|g_e|$:2.3–2.6 and $|g_h|$:0.3–0.6),[84–90] indicating the presence of environmental distortions and/or localization of the photogenerated carriers. It is important to note that while the Ni^{2+} doped $CsPb(Br_{1-x}Cl_x)_3$ NCs exhibited significant ODMR spectra, the corresponding undoped perovskite NCs remained devoid of magnetic resonance transitions, showing no ODMR signal. Such behavior can be attributed to the unique characteristics of these heterostructured materials, specifically their soft nature. The presence of an ODMR signal in the doped sample can be explained by the enhanced stabilization of the crystal skeleton through stronger Ni–Br/Cl interactions compared to Pb–Br/Cl interactions. This leads to a contraction of the octahedron sides and subsequently restricts the motion of the counterions. Based on the simulation of the spin manifold shown in Fig. 6(b) (with all relevant parameters listed in Table I), the presence of a sharp narrow peak was associated with an electron spin–flip (g_e = 1.998), whereas the broad peak was associated with a hole spin–flip (g_h = 1.12). The simulation of the excess broadening of the high-field resonance required consideration of the Ni^{2+} and hole exchange interaction ($J_{h\text{-}Ni}$). It should be noted that the simulations of the ODMR spectra were extremely sensitive to the value of $J_{h\text{-}Ni}$, providing evidence of a magnetic-exchange interaction between unpaired Ni^{2+} (S = 1) spins and the hole spin. The magnetic dopants exhibit a preferential interaction with hole spin, primarily due to the contribution of the s-orbitals of metal.

The Ni^{2+} doped halide perovskites were also examined for their dependence on the MW modulation frequencies similar to that performed for the II–VI nanocrystals. The spin-lattice relaxation time deduced from that measurement was found to be T_1 = 0.2 ms for an electron and T_1 = 0.75 ms for a hole.

In summary, the discussed results exposed, for the first time, carrier–dopant spin-exchange interaction in a lead-halide perovskite resembling that found in II–VI nanocrystals. The ODMR measurements uncovered the role of the dopant in localizing the photogenerated carriers by increasing the stiffness of the crystal structure. Furthermore, the ODMR data also revealed direct evidence of the hole–dopant interaction, resulting in an extended spin-lattice relaxation.

D. Cu-doped CdSe/CdS and $CuInS_2$ colloidal quantum dots

The interest in Cu-doped II–VI and Cu-based I–III–VI$_2$ QDs has grown significantly in recent years due to their desirable

optical features and the lack of toxic elements (in I–III–VI$_2$).[91–93] These properties make them ideal candidates for optoelectronic applications such as luminescent solar concentrators,[94–96] photovoltaic cells,[97] and low-threshold lasers.[98]

Numerous investigations have been conducted on copper-doped II–VI and copper-based I–III–VI$_2$ QDs. These studies have proposed various mechanisms to explain the luminescent behavior of these materials. One common mechanism for copper-doped II–VI QDs suggests a conduction-band electron recombining with a mid-gap trapped hole on a copper site, resembling metal-to-ligand (conduction band) charge-transfer $(ML_{(CB)}CT)$ processes.[99,100] This mechanism facilitates deep and broad emission with an extended lifetime attributed to the localized character of the copper-based hole. However, there is still ambiguity regarding the oxidation state of the incorporated copper dopants in the ground state, with some reports suggesting the presence of Cu^+ dopants[34,101] while others propose Cu^{2+} ions.[102,103]

Similar discussions surround the luminescence of copper-based I–III–VI$_2$ QDs. Some proposals suggest the existence of Cu^{2+} defects in the ground state of these QDs,[104–106] while others argue that the hole localizes at a Cu^+ site, which oxidizes to Cu^{2+}, leading to exciton self-trapping.[100,107] Meanwhile, other studies propose that the emission in $CuInS_2$ QDs involves a delocalized forbidden odd state in the valence band, resulting in deep and broad PL.[108] The Cu–In stoichiometry reveals more information on the recombination mechanism of $CuInS_2$ QD. Cu-rich compounds showed band-edge emission, while In-rich compounds showed deep emission.[109] Later on, it was proposed that the ratio of Cu to In determines the oxidation state of the copper, which in turn influences the recombination mechanism.[110]

In summary, the current understanding of the recombination mechanisms involved in Cu-doped and Cu-based materials is still somewhat limited and inconclusive. The investigation of the excited-state electronic structures and spin properties of copper-doped and copper-based QDs using ODMR spectroscopy has been limited.
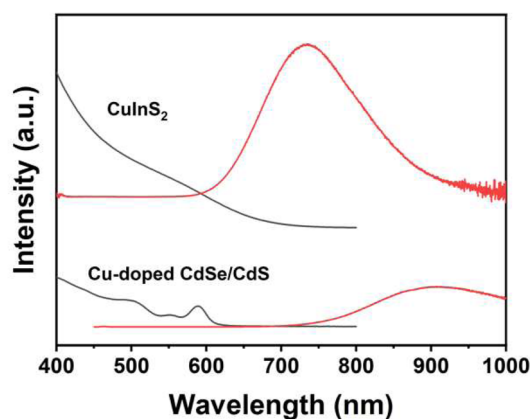
FIG. 7. Absorption (black) and photoluminescence (red) spectra of $CuInS_2$ and Cu-doped CdSe/CdS QDs at room temperature. Reproduced with permission from Harchol *et al.*, ACS Nano **16**, 12866–12877 (2022). Copyright 2022 American Chemical Society.

Using ODMR spectroscopy with theoretical modeling, it is possible to extract *g*-factors and spin relaxation times, which can give insights into the nature of the copper dopants, their oxidation states, and their interactions with the host lattice.

The undoped and Cu-doped CdSe/CdS and CuInS$_2$ QDs with and without ZnS or CdS shelling were synthesized by solution-based techniques, with procedures reported elsewhere.[96,111–113] We examined those materials using CW-ODMR spectroscopy at 2.5 K with different MW modulation frequencies. The spin properties were derived using a spin Hamiltonian model for the simulation of the CW-spectrum and a kinetic model for extracting transient variables (mainly the spin-lattice relaxation time, T$_1$).

The PL and absorption spectra at room temperature of the Cu-doped CdSe/CdS core–shell and CuInS$_2$ QDs are presented in Fig. 7. Both samples exhibit a single broadband in the PL spectrum, which is notably Stokes shifted from the absorption spectrum. Furthermore, the CuInS$_2$ QDs demonstrate slightly higher emission energy compared to the doped sample. Note that the CuInS$_2$ QDs with shelling exhibit the same red-shifted and broad PL spectrum.[49] Subsequently, these PL bands were further examined through ODMR spectroscopy.

The ODMR spectrum of Cu-doped CdSe/CdS QDs showed similar trends to those of undoped QDs, as depicted in Figs. 8(a) and 8(b). Both exhibited negative IP and positive OP signals, which could be further separated into broad and narrow sub-components [inset in Figs. 8(a) and 8(b)]. However, slight variations attributed to
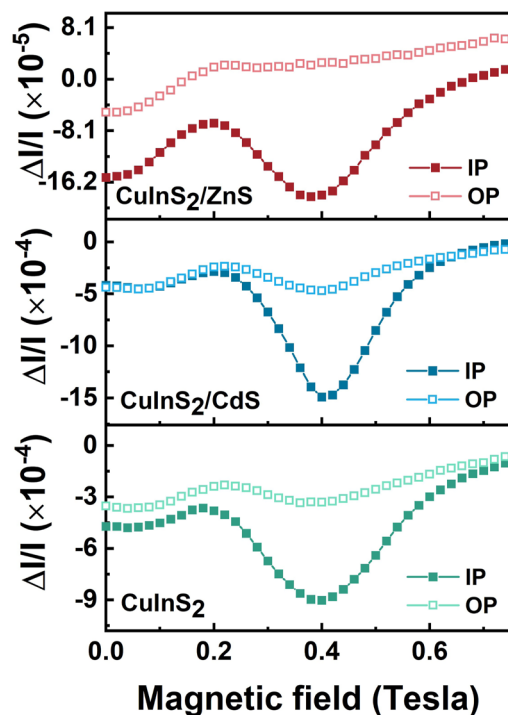
FIG. 9. CW-ODMR spectra of CuInS$_2$/ZnS (top), CuInS$_2$/CdS (middle), and CuInS$_2$ (bottom) QDs with a modulation frequency of 880 Hz. The measurements were acquired at 2.5 K under 405 nm laser excitation. (Reproduced with permission from Harchol *et al.*, ACS Nano **16**, 12866–12877 (2022). Copyright 2022 American Chemical Society.

copper impurities were noticeable, including differences in the width and position of these broad and narrow components.

Furthermore, the ODMR patterns observed for CuInS$_2$/ZnS, CuInS$_2$/CdS, and CuInS$_2$ QDs were found to be similar (Fig. 9), suggesting a correlation between the properties of the carriers and the CuInS$_2$ core. The IP ODMR spectrum of CuInS$_2$ exhibited a broad and negative resonance [yellow arrows in Fig. 2(b)], while the OP spectrum had reduced intensity, which indicated the localization of carriers and the involvement of paramagnetic centers with unpaired spins, such as Cu^{2+} with S = 1/2. Additionally, a low-field signal at 0.2 T was observed in the half-field of the central resonance, suggesting the presence of a triplet manifold [gray arrow in Fig. 2(b)]. The resonance positions and sub-components varied between the copper-doped and copper-based QDs, suggesting different recombination mechanisms.

The ODMR spectra of the Cu-doped CdSe/CdS and CuInS$_2$ QDs were measured at various MW modulation frequencies. The integrated areas under the ODMR curves, IP and OP, were determined for the narrow and broad components in the Cu-doped CdSe/CdS sample, as well as for the resonances at 0.4 and 0.2 T in the CuInS$_2$ sample. These areas were then plotted as a function of the MW modulation frequency, as shown in Figs. 10(a) and 10(b) for the Cu-doped and CuInS$_2$ QDs, respectively. The obtained trends were analyzed using a kinetic model, and the CW-ODMR spectra [Figs. 8(b) and 9] were simulated using a spin Hamiltonian, as
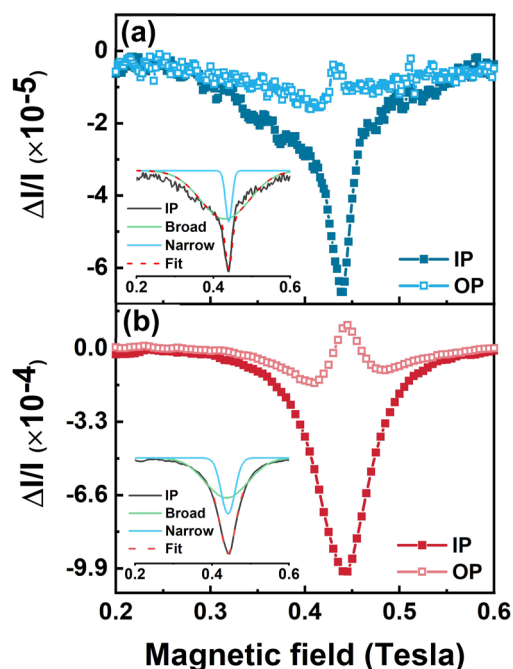

FIG. 8. ODMR spectra acquired at 2.5 K under 405 nm laser excitation with a MW modulation frequency of 880 Hz for (a) CdSe/CdS and (b) Cu doped CdSe/CdS QDs. The insets show the best fit obtained for the IP signal. Reproduced with permission from Harchol *et al.*, ACS Nano **16**, 12866–12877 (2022). Copyright 2022 American Chemical Society.
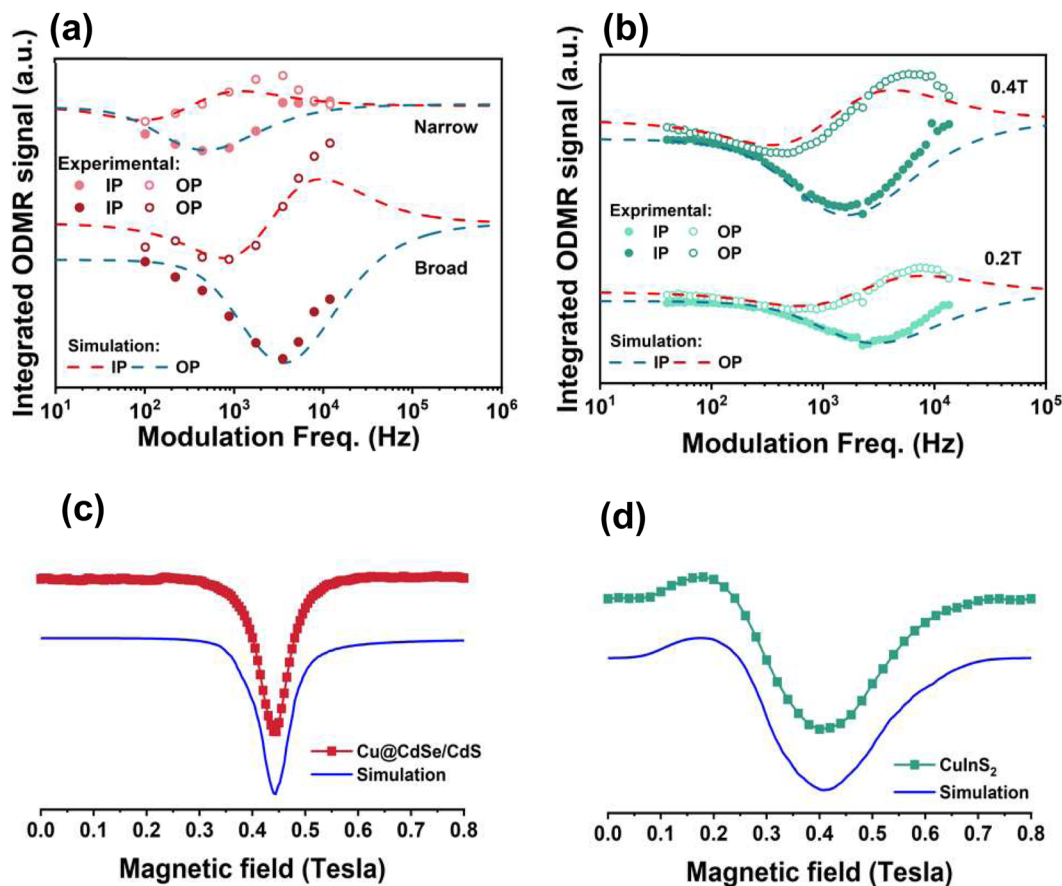
FIG. 10. Integrated ODMR signal (IP and OP) vs modulation frequency (log scale) for (a) Cu-doped CdSe/CdS and (b) CuInS$_2$ QDs. The red and blue dashed lines are fitted simulations to the IP and OP, respectively, according to the kinetic model shown in Eq. (4). ODMR spectra and fitted simulations (blue) of (c) Cu-doped CdSe/CdS and (d) CuInS$_2$ QDs. The simulations were calculated using the spin Hamiltonian in Eq. (1), and the fit parameters are presented in Table I. Reproduced with permission from Harchol *et al.*, ACS Nano **16**, 12866–12877 (2022). Copyright 2022 American Chemical Society.

described in Secs. II and V. The simulated spectra are compared to the experimental data in Figs. 10(a)–10(d), and the fitting parameters are summarized in Table I. For Cu-doped CdSe/CdS QDs, the ODMR spectrum indicated the presence of a conduction-band electron, a trapped hole, a weak electron–hole exchange interaction (J_{e-h} = 0.1 μeV), and a hyperfine interaction between the hole and the copper nuclei (A_{h-Cu} = 2.4 μeV). In contrast, the ODMR spectrum of the copper-based QDs suggested strong electron–hole exchange coupling (J_{e-h} = 1 meV), generating the singlet and triplet states with a minor axial zero-field splitting (D_{e-h} = 19 μeV). Figures 2(a) and 2(b) in Sec. II depict spin diagrams corresponding to Figs. 10(c) and 10(d), respectively. Therefore, in both the copper-doped and copper-based QDs, the hole is associated with a photogenerated Cu^{2+} site, and their differences relate to the extent of electron localization near this localized Cu^{2+} site.

Overall, the experimental results from the ODMR spectroscopy provided insights into the spin properties and recombination mechanisms of the copper-doped and copper-based QDs. The detailed analysis and interpretation of the ODMR spectra shed light on the structural and electronic properties of these nanomaterials, facilitating their further characterization and potential applications in optoelectronic devices.

IV. SUMMARY AND CONCLUSION

As magnetic doping in semiconductor nanocrystals has been implemented over the years, its relevance in manipulating nanocrystals' optical and magneto-optical properties has been realized. This article presents a few representative examples that have enabled the tackling of open questions regarding the coupling of individual host-carrier spins with dopant spins and the generation of new recombination pathways upon the inclusion of magnetic impurities. The investigation combines spectroscopic techniques, including PL and ODMR spectroscopy, to unravel physical parameters that have not been explored previously. Those parameters are summarized in Table I, highlighting their variability among different material platforms. The *g*-factor is particularly important among

the summarized parameters, providing information about the carrier type and its environment. The anisotropy in the g-factor values (along the principal axes directions x, y, and z) can reveal the location of the relevant carrier at an asymmetric site, potentially at surfaces or core/shell interfaces. Furthermore, the absolute value of the g-factor approaching that of a free carrier (2.00) can suggest detachment from a band-edge state, being free of influence by the orbital momentum (L ≠ 0) or/and spin–orbit coupling of the host material.

The exchange coupling constants between carriers (e, h) and dopant spins are also of paramount importance. As shown in Table I, the exchange interactions between the carrier and Mn dopant in both sNRs and NPLs fell within a similar range, ~10^{-1} meV. However, their characteristics differ. In the NPLs, the dominant exchange interaction involved the electron and Mn^{2+} (s–d exchange), whereas in the sNRs, it primarily occurred between a trapped hole in the core/shell interface and Mn^{2+} (p–d exchange). In most II–VI semiconductors, the p–d exchange interaction is 4–5 times stronger than the s–d interaction. However, in our case, this behavior is dictated by the distinct designs of the electronic band-edge, i.e., the wavefunction overlaps between the carrier and dopant. The NPLs possess a quasi-type-II band alignment, allowing the electron wave function to spread throughout the core/shell structure. On the other hand, the sNRs exhibit a type-I band alignment, concentrating the carrier near the interface. Note that, in the case of core/shell structures, the estimate of the number of dopant ions in close proximity to the interface supports the assumption of one-to-one carrier–dopant coupling.[47] Moreover, for Mn^{2+} in NPLs, the spread of the wave function into the shell induces additional coupling to the dopant's nuclear spins, as indicated by the non-zero hyperfine constant (A) in Table I.

Another intriguing observation is the spin exchange interaction between Ni^{2+} and the hole spin in halide perovskite NCs, which is reported for the first time. The selectivity concerning the hole in that material may originate from the s-orbit character of the hole and the lack of spin–orbit coupling at the valence band edge. For Ni^{2+} doped perovskites, the extracted value for the carrier–dopant interaction was found to be much weaker (~2 μeV) than in II–VI NCs. This weak exchange interaction can be attributed to generally weak s–d coupling and the instantaneous structural and electronic fluctuations inherent in soft perovskite materials.

In Cu-containing QDs, a Cu electronic state positioned deep within the bandgap plays a role in recombination emission. In Cu-doped CdSe/CdS, the Cu site traps a hole immediately after excitation, followed by the $ML_{CB}CT$ recombination singlet process. In $CuInS_2$, the study confirms that the trapped hole at a Cu site drags the counter electron, resulting in self-trapped excitons with a triplet recombination mechanism. Overall, magnetic ions manipulate the optical properties of semiconductor NCs through various routes.

Additionally, the study provides important insights into the spin-relaxation time (T_1). The findings indicate a trend of extension of the spin-relaxation time when the host-electron spin interacts with that of the dopant, compared to undoped counterparts. However, an exception to this trend is observed when nuclear coupling is involved, as seen in the case of Mn^{2+}-doped NPLs. This reversal in the spin-relaxation time highlights the complex interplay between different spin-related interactions.

In summary, the spin-related information revealed in the investigated materials provides a comprehensive understanding of the influence of dopants on the physics of semiconductor nanocrystals. This knowledge paves the way for implementing these materials in various spin-related technologies.

V. METHODS

Kinetic model. The kinetic model used in the above studies is presented in the following equation:

$$\frac{dn_s}{dt} = G_s - C_s n_s + k_{MW}(n_t - n_s) - k_{ISC}(n_s - F n_s)$$
$$+ k_{ISC}(n_t - (1 - F)n_t),$$
$$\frac{dn_t}{dt} = G_t - C_t n_t + k_{MW}(n_s - n_t) - k_{ISC}(n_t - (1 - F)n_t) \qquad (4)$$
$$+ k_{ISC}(n_s - F n_s)$$
$$F = \left(1 + e^{\frac{\Delta E}{kT}}\right)^{-1}; \quad C_{s,t} = r_{s,t} + d_{s,t}; \quad I \propto r_s n_s + r_t n_t,$$

where n_t and n_s represent the triplet populations (S = 1, m_S = ±1,0) and singlet (S = 0) spin sublevels, respectively. G_t and G_s are the generation rates, d_t and d_s are the dissociation rate constants, r_t and r_s represent the recombination rate constants, k_{MW} is the rate constant of the magnetic resonance transitions, k_{ISC} is the intersystem-crossing rate constant, F corresponds to a Fermi–Dirac thermal distribution function, and ΔE refers to the energy associated with a resonance transition. A few variables, like k_{ISC}, d_s, d_t, and r_t, were found to be negligible with respect to other dominant factors. Here, k_{MW} can be expressed as a function of the spin relaxation time, T_1. The value of T_1 was extracted from the extrema of the integrated OP signal. As explained in the main text, at this point, the MW modulation frequency is proportional to $1/T_1$.

PL and ODMR spectroscopy. ODMR measurements were carried out using a home-built ~10.8 GHz resonator with a window for laser irradiation placed in a Janis 12 CNDT liquid helium cryostat with a superconducting coil for magnetic field sweep. The magnetic field was controlled by an Oxford IPS 120 power supply. The sample was excited by a continuous-wave (CW) Laser diode with a wavelength of 405 nm. A microwave (MW) irradiation was generated by an HP 83620A source, triggered by a Stanford DG 535 pulse generator, and amplified by a Narda West 60583 MW amplifier. After excitation and magnetic resonance occurrence, the ODMR signal was passed through a 450/532 nm long-pass filter, inserted into a monochromator (SpectraPro 300i spectrometer), and detected with a Si-diode. The ODMR signal was recorded by an Ametek 7270 Lock-in amplifier referenced by on–off modulation of the MW (audio frequency of 0.02–20 kHz). ODMR experiments were performed in Voigt ($B_0 \perp$ excitation) and Faraday ($B_0 \parallel$ excitation) configurations, where a quarter waveplate and a linear polarizer were used to collect the right- and left-circularly polarized light in the latter. PL measurements were carried out in the same setup as the ODMR, using a chopper wheel to modulate the laser before excitation. The samples were sealed in quartz capillaries using Parafilm under ambient conditions. All ODMR simulations were performed using MATLAB code following the spin Hamiltonian in Eq. (1),

assuming the contribution of an ensemble of spins at 2.5 K under 10.8 GHz microwave irradiation.

AUTHOR DECLARATIONS

Conflict of Interest

The authors have no conflicts to disclose.

Author Contributions

J.D., A.H., and Y.B. contributed equally to this work.

Joanna Dehnel: Conceptualization (equal); Formal analysis (equal); Investigation (equal); Methodology (equal); Visualization (equal); Writing – original draft (equal); Writing – review & editing (equal). **Adi Harchol**: Conceptualization (equal); Formal analysis (equal); Investigation (equal); Methodology (equal); Visualization (equal); Writing – original draft (equal); Writing – review & editing (equal). **Yahel Barak**: Formal analysis (supporting); Investigation (equal); Methodology (equal); Visualization (equal); Writing – original draft (supporting); Writing – review & editing (supporting). **Itay Meir**: Formal analysis (supporting); Investigation (equal); Methodology (equal); Writing – review & editing (supporting). **Faris Horani**: Investigation (equal); Methodology (equal); Resources (equal); Visualization (equal); Writing – review & editing (supporting). **Arthur Shapiro**: Formal analysis (supporting); Investigation (equal); Methodology (equal). **Rotem Strassberg**: Formal analysis (supporting); Investigation (equal); Methodology (equal). **Celso de Mello Donegá**: Investigation (equal); Methodology (equal); Resources (equal); Writing – review & editing (supporting). **Hilmi Volkan Demir**: Funding acquisition (equal); Investigation (equal); Methodology (equal); Resources (equal); Writing – review & editing (supporting). **Daniel R. Gamelin**: Formal analysis (equal); Funding acquisition (equal); Investigation (equal); Methodology (equal); Resources (equal); Writing – review & editing (equal). **Kusha Sharma**: Conceptualization (equal); Formal analysis (equal); Methodology (equal); Supervision (supporting); Writing – original draft (supporting); Writing – review & editing (equal). **Efrat Lifshitz**: Conceptualization (equal); Data curation (equal); Formal analysis (equal); Funding acquisition (equal); Investigation (equal); Methodology (equal); Resources (equal); Supervision (lead); Writing – original draft (equal); Writing – review & editing (equal).

DATA AVAILABILITY

Data sharing is not applicable to this article as no new data were created or analyzed in this study.

REFERENCES

[1] R. Beaulac, S. T. Ochsenbein, and D. R. Gamelin, *Nanocrystal Quantum Dots*, 2nd ed., edited by V. I. Klimov (CRC Press, 2010).

[2] *Introduction to the Physics of Dilute Magnetic Semiconductors*, 1st ed., edited by J. A. Gaj and J. Kossut (Springer, Berlin, Heidelberg, 2010).

[3] S. C. Erwin, L. Zu, M. I. Haftel, A. L. Efros, T. A. Kennedy, and D. J. Norris, "Doping semiconductor nanocrystals," Nature **436**, 91–94 (2005).

[4] L. Besombes, Y. Léger, L. Maingault, D. Ferrand, H. Mariette, and J. Cibert, "Probing the spin state of a single magnetic ion in an individual quantum dot," Phys. Rev. Lett. **93**, 207403 (2004).

[5] L. Besombes, H. Boukari, C. Le Gall, A. Brunetti, C. L. Cao, S. Jamet, and B. Varghese, "Optical control of the spin of a magnetic atom in a semiconductor quantum dot," Nanophotonics **4**, 75–89 (2015).

[6] U. C. Mendes, M. Korkusinski, A. H. Trojnar, and P. Hawrylak, "Optical properties of charged quantum dots doped with a single magnetic impurity," Phys. Rev. B **88**, 115306 (2013).

[7] L. Cheng, C. Yuan, S. Shen, X. Yi, H. Gong, K. Yang, and Z. Liu, "Bottom-up synthesis of metal-ion-doped WS$_2$ nanoflakes for cancer theranostics," ACS Nano **9**, 11090–11101 (2015).

[8] F. Dolde, I. Jakobi, B. Naydenov, N. Zhao, S. Pezzagna, C. Trautmann, J. Meijer, P. Neumann, F. Jelezko, and J. Wrachtrup, "Room-temperature entanglement between single defect spins in diamond," Nat. Phys. **9**, 139–143 (2013).

[9] J. K. Furdyna, "Diluted magnetic semiconductors," J. Appl. Phys. **64**, R29–R64 (1988).

[10] R. Beaulac, L. Schneider, P. I. Archer, G. Bacher, and D. R. Gamelin, "Light-induced spontaneous magnetization in doped colloidal quantum dots," Science **325**, 973–976 (2009).

[11] R. Beaulac, P. I. Archer, J. van Rijssel, A. Meijerink, and D. R. Gamelin, "Exciton storage by Mn^{2+} in colloidal Mn^{2+}-doped CdSe quantum dots," Nano Lett. **8**, 2949–2953 (2008).

[12] H. D. Nelson, L. R. Bradshaw, C. J. Barrows, V. A. Vlaskin, and D. R. Gamelin, "Picosecond dynamics of excitonic magnetic polarons in colloidal diffusion-doped Cd$_{1-x}$Mn$_x$Se quantum dots," ACS Nano **9**, 11177–11191 (2015).

[13] R. Beaulac, P. I. Archer, S. T. Ochsenbein, and D. R. Gamelin, "Mn^{2+}-doped CdSe quantum dots: New inorganic materials for spin-electronics and spin-photonics," Adv. Funct. Mater. **18**, 3873–3891 (2008).

[14] M. Nirmal, D. J. Norris, M. Kuno, M. G. Bawendi, A. L. Efros, and M. Rosen, "Observation of the "dark exciton" in CdSe quantum dots," Phys. Rev. Lett. **75**, 3728–3731 (1995).

[15] C. de Mello Donegá, M. Bode, and A. Meijerink, "Size- and temperature-dependence of exciton lifetimes in CdSe quantum dots," Phys. Rev. B **74**, 085320 (2006).

[16] C. J. Barrows, V. A. Vlaskin, and D. R. Gamelin, "Absorption and magnetic circular dichroism analyses of giant Zeeman splittings in diffusion-doped colloidal Cd$_{1-x}$Mn$_x$Se quantum dots," J. Phys. Chem. Lett. **6**, 3076–3081 (2015).

[17] D. A. Bussian, S. A. Crooker, M. Yin, M. Brynda, A. L. Efros, and V. I. Klimov, "Tunable magnetic exchange interactions in manganese-doped inverted core–shell ZnSe–CdSe nanocrystals," Nat. Mater. **8**, 35–40 (2009).

[18] N. Grumbach, A. Rubin-Brusilovski, G. I. Maikov, E. Tilchin, and E. Lifshitz, "Manipulation of carrier–Mn^{2+} exchange interaction in CdTe/CdSe colloidal quantum dots by controlled positioning of Mn^{2+} impurities," J. Phys. Chem. C **117**, 21021–21027 (2013).

[19] K. M. Hanif, R. W. Meulenberg, and G. F. Strouse, "Magnetic ordering in doped $Cd_{1-x}Co_xSe$ diluted magnetic quantum dots," J. Am. Chem. Soc. **124**, 11495–11502 (2002).

[20] L. De Trizio, M. Prato, A. Genovese, A. Casu, M. Povia, R. Simonutti, M. J. P. Alcocer, C. D'Andrea, F. Tassone, and L. Manna, "Strongly fluorescent quaternary Cu–In–Zn–S nanocrystals prepared from $Cu_{1-x}InS_2$ nanocrystals by partial cation exchange," Chem. Mater. **24**, 2400–2406 (2012).

[21] V. A. Vlaskin, C. J. Barrows, C. S. Erickson, and D. R. Gamelin, "Nanocrystal diffusion doping," J. Am. Chem. Soc. **135**, 14380–14389 (2013).

[22] Y. Yang, O. Chen, A. Angerhofer, and Y. C. Cao, "On doping CdS/ZnS core/shell nanocrystals with Mn," J. Am. Chem. Soc. **130**, 15649–15661 (2008).

[23] I. A. Merkulov, D. R. Yakovlev, A. Keller, W. Ossau, J. Geurts, A. Waag, G. Landwehr, G. Karczewski, T. Wojtowicz, and J. Kossut, "Kinetic exchange between the conduction band electrons and magnetic ions in quantum-confined structures," Phys. Rev. Lett. **83**, 1431–1434 (1999).

[24] R. Beaulac, Y. Feng, J. W. May, E. Badaeva, D. R. Gamelin, and X. Li, "Orbital pathways for Mn^{2+}-carrier sp-d exchange in diluted magnetic semiconductor quantum dots," Phys. Rev. B **84**, 195324 (2011).

[25] S. T. Ochsenbein and D. R. Gamelin, "Quantum oscillations in magnetically doped colloidal nanocrystals," Nat. Nanotechnol. **6**, 112–115 (2011).

[26] L. Besombes, Y. Leger, L. Maingault, D. Ferrand, H. Mariette, and J. Cibert, "Carrier-induced spin splitting of an individual magnetic atom embedded in a quantum dot," Phys. Rev. B **71**, 161307 (2005).

[27] M. M. Glazov, E. L. Ivchenko, L. Besombes, Y. Léger, L. Maingault, and H. Mariette, "Fine structure of exciton excited levels in a quantum dot with a magnetic ion," Phys. Rev. B **75**, 205313 (2007).

[28] J. Kossut and W. Dobrowolski, *Handbook of Magnetic Materials*, edited by K. H. J. Buschow (Elsevier Science, 1993), Chap. 4, Vol. 7.

[29] P. Kacman, "Spin interactions in diluted magnetic semiconductors and magnetic semiconductor structures," Semicond. Sci. Technol. **16**, R25 (2001).

[30] V. Tiwari, M. Arino, S. Gupta, M. Morita, T. Inoue, D. Caliste, P. Pochet, H. Boukari, S. Kuroda, and L. Besombes, "Hole-Cr^+ nanomagnet in a semiconductor quantum dot," Phys. Rev. B **104**, L041301 (2021).

[31] W. Mac, A. Twardowski, and M. S. Demianiuk, "s,p-d exchange interaction in Cr-based diluted magnetic semiconductors," Phys. Rev. B **54**, 5528–5535 (1996).

[32] R. Beaulac, P. I. Archer, and D. R. Gamelin, "Luminescence in colloidal Mn^{2+}-doped semiconductor nanocrystals," J. Solid State Chem. **181**, 1582–1589 (2008).

[33] R. Beaulac, P. I. Archer, X. Liu, S. Lee, G. M. Salley, M. Dobrowolska, J. K. Furdyna, and D. R. Gamelin, "Spin-polarizable excitonic luminescence in colloidal Mn^{2+}-doped CdSe quantum dots," Nano Lett. **8**, 1197–1201 (2008).

[34] B. B. Srivastava, S. Jana, and N. Pradhan, "Doping Cu in semiconductor nanocrystals: Some old and some new physical insights," J. Am. Chem. Soc. **133**, 1007–1015 (2011).

[35] S. Brovelli, C. Galland, R. Viswanatha, and V. I. Klimov, "Tuning radiative recombination in Cu-doped nanocrystals via electrochemical control of surface trapping," Nano Lett. **12**, 4372–4379 (2012).

[36] P. J. Whitham, K. E. Knowles, P. J. Reid, and D. R. Gamelin, "Photoluminescence blinking and reversible electron trapping in copper-doped CdSe nanocrystals," Nano Lett. **15**, 4045–4051 (2015).

[37] D. J. Norris, N. Yao, F. T. Charnock, and T. A. Kennedy, "High-quality manganese-doped ZnSe nanocrystals," Nano Lett. **1**, 3–7 (2001).

[38] R. Fainblat, J. Frohleiks, F. Muckel, J. H. Yu, J. Yang, T. Hyeon, and G. Bacher, "Quantum confinement-controlled exchange coupling in manganese(II)-doped CdSe two-dimensional quantum well nanoribbons," Nano Lett. **12**, 5311–5317 (2012).

[39] J. R. Murphy, S. Delikanli, T. Scrace, P. Zhang, T. Norden, T. Thomay, A. N. Cartwright, H. V. Demir, and A. Petrou, "Time-resolved photoluminescence study of CdSe/CdMnS/CdS core/multi-shell nanoplatelets," Appl. Phys. Lett. **108**, 242406 (2016).

[40] P. I. Archer, S. A. Santangelo, and D. R. Gamelin, "Direct observation of sp-d exchange interactions in colloidal Mn^{2+}- and Co^{2+}-doped CdSe quantum dots," Nano Lett. **7**, 1037–1043 (2007).

[41] G. Bacher, L. Schneider, R. Beaulac, P. I. Archer, and D. R. Gamelin, "Magnetic polaron formation dynamics in Mn^{2+}-doped colloidal nanocrystals up to room temperature," J. Korean Phys. Soc. **58**, 1261–1266 (2011).

[42] L. Besombes, Y. Leger, J. Bernos, H. Boukari, H. Mariette, J. P. Poizat, T. Clement, J. Fernández-Rossier, and R. Aguado, "Optical probing of spin fluctuations of a single paramagnetic Mn atom in a semiconductor quantum dot," Phys. Rev. B **78**, 125324 (2008).

[43] W. D. Rice, W. Liu, T. A. Baker, N. A. Sinitsyn, V. I. Klimov, and S. A. Crooker, "Revealing giant internal magnetic fields due to spin fluctuations in magnetically doped colloidal nanocrystals," Nat. Nanotechnol. **11**, 137–142 (2016).

[44] L. R. Bradshaw, J. W. May, J. L. Dempsey, X. Li, and D. R. Gamelin, "Ferromagnetic excited-state Mn^{2+} dimers in $Zn_{1-x}Mn_xSe$ quantum dots observed by time-resolved magnetophotoluminescence," Phys. Rev. B **89**, 115312 (2014).

[45] L. Besombes, C. L. Cao, S. Jamet, H. Boukari, and J. Fernandez-Rossier, "Optical control of the spin state of two Mn atoms in a quantum dot," Phys. Rev. B **86**, 165306 (2012).

[46] J. Dehnel, Y. Barak, I. Meir, A. K. Budniak, A. P. Nagvenkar, D. R. Gamelin, and E. Lifshitz, "Insight into the spin properties in undoped and Mn-doped CdSe/CdS-seeded nanorods by optically detected magnetic resonance," ACS Nano **14**, 13478–13490 (2020).

[47] R. Strassberg, S. Delikanli, Y. Barak, J. Dehnel, A. Kostadinov, G. Maikov, P. L. Hernandez-Martinez, M. Sharma, H. V. Demir, and E. Lifshitz, "Persuasive evidence for electron-nuclear coupling in diluted magnetic colloidal nanoplatelets using optically detected magnetic resonance spectroscopy," J. Phys. Chem. Lett. **10**, 4437–4447 (2019).

[48] Y. Barak, I. Meir, J. Dehnel, F. Horani, D. R. Gamelin, A. Shapiro, and E. Lifshitz, "Uncovering the influence of Ni^{2+} doping in lead-halide perovskite nanocrystals using optically detected magnetic resonance spectroscopy," Chem. Mater. **34**, 1686–1698 (2022).

[49] A. Harchol, Y. Barak, K. E. Hughes, K. H. Hartstein, H. j. Jöbsis, P. T. Prins, C. de Mello Donegá, D. R. Gamelin, and E. Lifshitz, "Optically detected magnetic resonance spectroscopy of Cu-doped CdSe/CdS and $CuInS_2$ colloidal quantum dots," ACS Nano **16**, 12866–12877 (2022).

[50] E. Lifshitz, L. Fradkin, A. Glozman, and L. Langof, "Optically detected magnetic resonance studies of colloidal semiconductor nanocrystals," Annu. Rev. Phys. Chem. **55**, 509–557 (2004).

[51] S. Y. Lee, S. Paik, D. R. McCamey, and C. Boehme, "Modulation frequency dependence of continuous-wave optically/electrically detected magnetic resonance," Phys. Rev. B **86**, 115204 (2012).

[52] M. Zavelani-Rossi, M. G. Lupo, F. Tassone, L. Manna, and G. Lanzani, "Suppression of biexciton Auger recombination in CdSe/CdS dot/rods: Role of the electronic structure in the carrier dynamics," Nano Lett. **10**, 3142–3150 (2010).

[53] F. T. Rabouw, P. Lunnemann, R. J. A. van Dijk-Moes, M. Frimmer, F. Pietra, A. F. Koenderink, and D. D. Vanmaekelbergh, "Reduced Auger recombination in single CdSe/CdS nanorods by one-dimensional electron delocalization," Nano Lett. **13**, 4884–4892 (2013).

[54] L. Carbone, C. Nobile, M. De Giorgi, F. D. Sala, G. Morello, P. Pompa, M. Hytch, E. Snoeck, A. Fiore, I. R. Franchini, M. Nadasan, A. F. Silvestre, L. Chiodo, S. Kudera, R. Cingolani, R. Krahne, and L. Manna, "Synthesis and micrometer-scale assembly of colloidal CdSe/CdS nanorods prepared by a seeded growth approach," Nano Lett. **7**, 2942–2950 (2007).

[55] A. Sitt, F. D. Sala, G. Menagen, and U. Banin, "Multiexciton engineering in seeded core/shell nanorods: Transfer from type-I to quasi-type-II regimes," Nano Lett. **9**, 3470–3476 (2009).

[56] B. Siebers, L. Biadala, D. R. Yakovlev, A. V. Rodina, T. Aubert, Z. Hens, and M. Bayer, "Exciton spin dynamics and photoluminescence polarization of CdSe/CdS dot-in-rod nanocrystals in high magnetic fields," Phys. Rev. B **91**, 155304 (2015).

[57] A. Granados Del Águila, B. Jha, F. Pietra, E. Groeneveld, C. de Mello Donegá, J. C. Maan, D. Vanmaekelbergh, and P. C. M. Christianen, "Observation of the full exciton and phonon fine structure in CdSe/CdS dot-in-rod heteronanocrystals," ACS Nano **8**, 5921–5931 (2014).

[58] K. J. van Schooten, J. Huang, D. V. Talapin, C. Boehme, and J. M. Lupton, "Spin-dependent electronic processes and long-lived spin coherence of deep-level trap sites in CdS nanocrystals," Phys. Rev. B **87**, 125412 (2013).

[59] K. J. van Schooten, J. Huang, W. J. Baker, D. V. Talapin, C. Boehme, and J. M. Lupton, "Spin-dependent exciton quenching and spin coherence in CdSe/CdS nanocrystals," Nano Lett. **13**, 65–71 (2013).

21 August 2023 10:07:44

[60] S. Delikanli, G. Yu, A. Yeltik, S. Bose, T. Erdem, J. Yu, O. Erdem, M. Sharma, V. K. Sharma, U. Quliyeva, S. Shendre, C. Dang, D. H. Zhang, T. C. Sum, W. Fan, and H. V. Demir, "Ultrathin highly luminescent two-monolayer colloidal CdSe nanoplatelets," Adv. Funct. Mater. **29**, 1901028 (2019).

[61] S. Ithurria and B. Dubertret, "Quasi 2D colloidal CdSe platelets with thicknesses controlled at the atomic level," J. Am. Chem. Soc. **130**, 16504–16505 (2008).

[62] S. Delikanli, M. Z. Akgul, J. R. Murphy, B. Barman, Y. Tsai, T. Scrace, P. Zhang, B. Bozok, P. L. Hernández-Martínez, J. Christodoulides, A. N. Cartwright, A. Petrou, and H. V. Demir, "Mn^{2+}-doped CdSe/CdS core/multishell colloidal quantum wells enabling tunable carrier-dopant exchange interactions," ACS Nano **9**(12), 12473–12479 (2015).

[63] J. H. Yu, X. Liu, K. E. Kweon, J. Joo, J. Park, K. T. Ko, D. W. Lee, S. Shen, K. Tivakornsasithorn, J. S. Son, J. H. Park, Y. W. Kim, G. S. Hwang, M. Dobrowolska, J. K. Furdyna, and T. Hyeon, "Giant Zeeman splitting in nucleation-controlled doped $CdSe:Mn^{2+}$ quantum nanoribbons," Nat. Mater. **9**, 47–53 (2010).

[64] I. D. Litvin, H. Porteanu, E. Lifshitz, and A. A. Lipovskii, "Optically detected magnetic resonance studies of CdS nanoparticles grown in phosphate glass," J. Cryst. Growth **198–199**, 313–315 (1999).

[65] D. R. Ceratti, Y. Rakita, L. Cremonesi, R. Tenne, V. Kalchenko, M. Elbaum, D. Oron, M. A. C. Potenza, G. Hodes, and D. Cahen, "Self-healing inside $APbBr_3$ halide perovskite crystals," Adv. Mater. **30**, 1706273 (2018).

[66] J. Kang and L. W. Wang, "High defect tolerance in lead halide perovskite $CsPbBr_3$," J. Phys. Chem. Lett. **8**, 489–493 (2017).

[67] H. Huang, M. I. Bodnarchuk, S. V. Kershaw, M. V. Kovalenko, and A. L. Rogach, "Lead halide perovskite nanocrystals in the research spotlight: Stability and defect tolerance," ACS Energy Lett. **2**, 2071–2083 (2017).

[68] A. V. Cohen, D. A. Egger, A. M. Rappe, and L. Kronik, "Breakdown of the static picture of defect energetics in halide perovskites: The case of the Br vacancy in $CsPbBr_3$," J. Phys. Chem. Lett. **10**, 4490–4498 (2019).

[69] A. A. Zhumekenov, M. I. Saidaminov, M. A. Haque, E. Alarousu, S. P. Sarmah, B. Murali, I. Dursun, X. H. Miao, A. L. Abdelhady, T. Wu, O. F. Mohammed, and O. M. Bakr, "Formamidinium lead halide perovskite crystals with unprecedented long carrier dynamics and diffusion length," ACS Energy Lett. **1**, 32–37 (2016).

[70] L. Protesescu, S. Yakunin, M. I. Bodnarchuk, F. Krieg, R. Caputo, C. H. Hendon, R. X. Yang, A. Walsh, and M. V. Kovalenko, "Nanocrystals of cesium lead halide perovskites ($CsPbX_3$, X = Cl, Br, and I): Novel optoelectronic materials showing bright emission with wide color gamut," Nano Lett. **15**, 3692–3696 (2015).

[71] M. Z. Mayers, L. Z. Tan, D. A. Egger, A. M. Rappe, and D. R. Reichman, "How lattice and charge fluctuations control carrier dynamics in halide perovskites," Nano Lett. **18**, 8041–8046 (2018).

[72] A. D. Wright, C. Verdi, R. L. Milot, G. E. Eperon, M. A. Pérez-Osorio, H. J. Snaith, F. Giustino, M. B. Johnston, and L. M. Herz, "Electron-phonon coupling in hybrid lead halide perovskites," Nat. Commun. **7**, 11755 (2016).

[73] J. S. Yao, J. Ge, B. N. Han, K. H. Wang, H. B. Yao, H. L. Yu, J. H. Li, B. S. Zhu, J. Z. Song, C. Chen, Q. Zhang, H. B. Zeng, Y. Luo, and S. H. Yu, "Ce^{3+}-doping to modulate photoluminescence kinetics for efficient $CsPbBr_3$ nanocrystals based light-emitting diodes," J. Am. Chem. Soc. **140**, 3626–3634 (2018).

[74] W. J. Mir, A. Swarnkar, and A. Nag, "Postsynthesis Mn-doping in $CsPbI_3$ nanocrystals to stabilize the black perovskite phase," Nanoscale **11**, 4278–4286 (2019).

[75] S. Zhou, Y. Zhu, J. Zhong, F. Tian, H. Huang, J. Chen, and D. Chen, "Chlorine-additive-promoted incorporation of Mn^{2+} dopants into $CsPbCl_3$ perovskite nanocrystals," Nanoscale **11**, 12465–12470 (2019).

[76] Z. Chen, H. Chen, C. Zhang, L. Chen, Z. Qin, H. Sang, X. Wang, and M. Xiao, "Excitation-tailored dual-color emission of manganese(II)-doped perovskite nanocrystals," Appl. Phys. Lett. **114**, 041902 (2019).

[77] S. Wang, J. Leng, Y. Yin, J. Liu, K. Wu, and S. Jin, "Ultrafast dopant-induced exciton Auger-like recombination in Mn-doped perovskite nanocrystals," ACS Energy Lett. **5**, 328–334 (2020).

[78] Z. Fang, M. Shang, X. Hou, Y. Zheng, Z. Du, Z. Yang, K. C. Chou, W. Yang, Z. L. Wang, and Y. Yang, "Bandgap alignment of α-$CsPbI_3$ perovskites with synergistically enhanced stability and optical performance via B-site minor doping," Nano Energy **61**, 389–396 (2019).

[79] A. Shapiro, M. W. Heindl, F. Horani, M.-H. Dahan, J. Tang, Y. Amouyal, and E. Lifshitz, "Significance of Ni doping in $CsPbX_3$ nanocrystals via postsynthesis cation–anion coexchange," J. Phys. Chem. C **123**, 24979–24987 (2019).

[80] G. H. Ahmed, J. Yin, O. M. Bakr, and O. F. Mohammed, "Near-unity photoluminescence quantum yield in inorganic perovskite nanocrystals by metal-ion doping," J. Chem. Phys. **152**, 020902 (2020).

[81] Z. Yong, S. Guo, J.-P. Ma, J.-Y. Zhang, Z. Li, Y. Chen, B. Zhang, Y. Zhou, J. Shu, J. Gu, L. Zheng, O. M. Bakr, and H. Sun, "Doping-enhanced short-range order of perovskite nanocrystals for near-unity violet luminescence quantum yield," J. Am. Chem. Soc. **140**, 9942–9951 (2018).

[82] R. K. Behera, A. Dutta, D. Ghosh, S. Bera, S. Bhattacharyya, and N. Pradhan, "Doping the smallest Shannon radii transition metal ion Ni(II) for stabilizing α-$CsPbI_3$ perovskite nanocrystals," J. Phys. Chem. Lett. **10**, 7916–7921 (2019).

[83] K. Xing, X. Yuan, Y. Wang, J. Li, Y. Wang, Y. Fan, L. Yuan, K. Li, Z. Wu, H. Li, and J. Zhao, "Improved doping and emission efficiencies of Mn-doped $CsPbCl_3$ perovskite nanocrystals via nickel chloride," J. Phys. Chem. Lett. **10**, 4177–4184 (2019).

[84] C. Zhang, D. Sun, C.-X. Sheng, Y. X. Zhai, K. Mielczarek, A. Zakhidov, and Z. V. Vardeny, "Magnetic field effects in hybrid perovskite devices," Nat. Phys. **11**, 427–434 (2015).

[85] X. Liu, A. Chanana, U. Huynh, F. Xue, P. Haney, S. Blair, X. Jiang, and Z. V. Vardeny, "Circular photogalvanic spectroscopy of Rashba splitting in 2D hybrid organic–inorganic perovskite multiple quantum wells," Nat. Commun. **11**, 323 (2020).

[86] J. Wang, C. Zhang, H. Liu, R. McLaughlin, Y. Zhai, S. R. Vardeny, X. Liu, S. McGill, D. Semenov, H. Guo, R. Tsuchikawa, V. V. Deshpande, D. Sun, and Z. V. Vardeny, "Spin-optoelectronic devices based on hybrid organic-inorganic trihalide perovskites," Nat. Commun. **10**, 129 (2019).

[87] P. Odenthal, W. Talmadge, N. Gundlach, R. Wang, C. Zhang, D. Sun, Z.-G. Yu, Z. Valy Vardeny, and Y. S. Li, "Spin-polarized exciton quantum beating in hybrid organic–inorganic perovskites," Nat. Phys. **13**, 894–899 (2017).

[88] V. V. Belykh, D. R. Yakovlev, M. M. Glazov, P. S. Grigoryev, M. Hussain, J. Rautert, D. N. Dirin, M. V. Kovalenko, and M. Bayer, "Coherent spin dynamics of electrons and holes in $CsPbBr_3$ perovskite crystals," Nat. Commun. **10**, 673 (2019).

[89] M. J. Crane, L. M. Jacoby, T. A. Cohen, Y. Huang, C. K. Luscombe, and D. R. Gamelin, "Coherent spin precession and lifetime-limited spin dephasing in $CsPbBr_3$ perovskite nanocrystals," Nano Lett. **20**, 8626–8633 (2020).

[90] H. Utzat, W. Sun, A. E. K. Kaplan, F. Krieg, M. Ginterseder, B. Spokoyny, N. D. Klein, K. E. Shulenberger, C. F. Perkinson, M. V. Kovalenko, and M. G. Bawendi, "Coherent single-photon emission from colloidal lead halide perovskite quantum dots," Science **363**, 1068–1072 (2019).

[91] K. E. Knowles, K. H. Hartstein, T. B. Kilburn, A. Marchioro, H. D. Nelson, P. J. Whitham, and D. R. Gamelin, "Luminescent colloidal semiconductor nanocrystals containing copper: Synthesis, photophysics, and applications," Chem. Rev. **116**, 10820–10851 (2016).

[92] W. van der Stam, A. C. Berends, and C. de Mello Donega, "Prospects of colloidal copper chalcogenide nanocrystals," ChemPhysChem **17**, 559–581 (2016).

[93] A. C. Berends, M. J. J. Mangnus, C. Xia, F. T. Rabouw, and C. de Mello Donega, "Optoelectronic properties of ternary I–III–VI₂ semiconductor nanocrystals: Bright prospects with elusive origins," J. Phys. Chem. Lett. **10**, 1600–1616 (2019).

[94] L. R. Bradshaw, K. E. Knowles, S. McDowall, and D. R. Gamelin, "Nanocrystals for luminescent solar concentrators," Nano Lett. **15**, 1315–1323 (2015).

[95] F. Meinardi, H. McDaniel, F. Carulli, A. Colombo, K. A. Velizhanin, N. S. Makarov, R. Simonutti, V. I. Klimov, and S. Brovelli, "Highly efficient large-area colourless luminescent solar concentrators using heavy-metal-free colloidal quantum dots," Nat. Nanotechnol. **10**, 878–885 (2015).

[96] K. E. Knowles, T. B. Kilburn, D. G. Alzate, S. McDowall, and D. R. Gamelin, "Bright $CuInS_2$/CdS nanocrystal phosphors for high-gain full-spectrum luminescent solar concentrators," Chem. Commun. **51**, 9129–9132 (2015).

[97] M. G. Panthani, V. Akhavan, B. Goodfellow, J. P. Schmidtke, L. Dunn, A. Dodabalapur, P. F. Barbara, and B. A. Korgel, "Synthesis of $CuInS_2$, $CuInSe_2$, and $Cu(In_xGa_{1-x})Se_2$ (CIGS) nanocrystal "inks" for printable photovoltaics," J. Am. Chem. Soc. **130**, 16770–16777 (2008).

[98] J. Yu, M. Sharma, M. Li, S. Delikanli, A. Sharma, M. Taimoor, Y. Altintas, J. R. McBride, T. Kusserow, T. C. Sum, H. V. Demir, and C. Dang, "Low-threshold

lasing from copper-doped CdSe colloidal quantum wells," Laser Photonics Rev. **15**, 2100034 (2021).

[99] A. N. Yadav, A. K. Singh, D. Chauhan, P. R. Solanki, P. Kumar, and K. Singh, "Evaluation of dopant energy and Stokes shift in Cu-doped CdS quantum dots: Via spectro-electrochemical probing," New J. Chem. **44**, 13529–13533 (2020).

[100] K. E. Knowles, H. D. Nelson, T. B. Kilburn, and D. R. Gamelin, "Singlet-triplet splittings in the luminescent excited states of colloidal Cu^+:CdSe, Cu^+:InP, and $CuInS_2$ nanocrystals: Charge-transfer configurations and self-trapped excitons," J. Am. Chem. Soc. **137**, 13138–13147 (2015).

[101] C. Corrado, Y. Jiang, F. Oba, M. Kozina, F. Bridges, and J. Z. Zhang, "Synthesis, structural, and optical properties of stable ZnS:Cu,Cl nanocrystals," J. Phys. Chem. A **113**, 3830–3839 (2009).

[102] R. Viswanatha, S. Brovelli, A. Pandey, S. A. Crooker, and V. I. Klimov, "Copper-doped inverted core/shell nanocrystals with "permanent" optically active holes," Nano Lett. **11**, 4753–4758 (2011).

[103] G. K. Grandhi, R. Tomar, and R. Viswanatha, "Study of surface and bulk electronic structure of II–VI semiconductor nanocrystals using Cu as a nanosensor," ACS Nano **6**, 9751–9763 (2012).

[104] W. D. Rice, H. Mcdaniel, V. I. Klimov, and S. A. Crooker, "Magneto-optical properties of $CuInS_2$ nanocrystals," J. Phys. Chem. Lett. **5**, 4105–4109 (2014).

[105] A. S. Fuhr, H. J. Yun, N. S. Makarov, H. Li, H. McDaniel, and V. I. Klimov, "Light emission mechanisms in $CuInS_2$ quantum dots evaluated by spectral electrochemistry," ACS Photonics **4**, 2425–2435 (2017).

[106] V. Pinchetti, M. Lorenzon, H. McDaniel, R. Lorenzi, F. Meinardi, V. I. Klimov, and S. Brovelli, "Spectro-electrochemical probing of intrinsic and extrinsic processes in exciton recombination in I-III-VI$_2$ nanocrystals," Nano Lett. **17**, 4508–4517 (2017).

[107] A. C. Berends, F. T. Rabouw, F. C. M. Spoor, E. Bladt, F. C. Grozema, A. J. Houtepen, L. D. A. Siebbeles, and C. de Mello Donegá, "Radiative and non-radiative recombination in $CuInS_2$ nanocrystals and $CuInS_2$-based core/shell nanocrystals," J. Phys. Chem. Lett. **7**, 3503–3509 (2016).

[108] A. Shabaev, M. J. Mehl, and A. L. Efros, "Energy band structure of $CuInS_2$ and optical spectra of $CuInS_2$ nanocrystals," Phys. Rev. B **92**, 035431 (2015).

[109] D. H. Jara, K. G. Stamplecoskie, and P. V. Kamat, "Two distinct transitions in Cu_xInS_2 quantum dots. Bandgap versus sub-bandgap excitations in copper-deficient structures," J. Phys. Chem. Lett. **7**, 1452–1459 (2016).

[110] A. Fuhr, H. J. Yun, S. A. Crooker, and V. I. Klimov, "Spectroscopic and magneto-optical signatures of Cu^{1+} and Cu^{2+} defects in copper indium sulfide quantum dots," ACS Nano **14**, 2212–2223 (2020).

[111] C. Xia, P. Tamarat, L. Hou, S. Busatto, J. D. Meeldijk, C. de Mello Donega, and B. Lounis, "Unraveling the emission pathways in copper indium sulfide quantum dots," ACS Nano **15**, 17573–17581 (2021).

[112] S. O. M. Hinterding, M. J. J. Mangnus, P. T. Prins, H. J. Jöbsis, S. Busatto, D. Vanmaekelbergh, C. de Mello Donega, and F. T. Rabouw, "Unusual spectral diffusion of single $CuInS_2$ quantum dots sheds light on the mechanism of radiative decay," Nano Lett. **21**, 658–665 (2021).

[113] K. E. Hughes, K. H. Hartstein, and D. R. Gamelin, "Photodoping and transient spectroscopies of copper-doped CdSe/CdS nanocrystals," ACS Nano **12**, 718–728 (2018).